Monthly Notices
of the
ROYAL ASTRONOMICAL SOCIETY

MNRAS **482,** 929–949 (2019)
Advance Access publication 2018 October 11

doi:10.1093/mnras/sty2745

Modelling long-period variables – I. A new grid of O-rich and C-rich pulsation models

Michele Trabucchi,[1]★ Peter R. Wood,[2] Josefina Montalbán,[1] Paola Marigo,[1]
Giada Pastorelli[1] and Léo Girardi[3]

[1]*Dipartimento di Fisica e Astronomia, Università di Padova, Vicolo dell'Osservatorio 2, I-35122 Padova, Italy*
[2]*Research School of Astronomy and Astrophysics, Australian National University, Canberra, ACT2611, Australia*
[3]*Osservatorio Astronomico di Padova – INAF, Vicolo dell'Osservatorio 5, I-35122 Padova, Italy*

Accepted 2018 October 5. Received 2018 October 3; in original form 2018 September 19

ABSTRACT

We present a new grid of non-adiabatic, linear pulsation models of long-period variables (LPVs), including periods and growth rates for radial modes from the fundamental to the fourth overtone. The models span a wide range in mass, luminosity, metallicity, C/O ratio, and helium abundance, effectively covering the whole thermally pulsing asymptotic giant branch (TP-AGB) evolution, and representing a significant update with respect to previous works. The main improvement is the inclusion of detailed atomic and molecular opacities, consistent with the models chemical mixture, that makes the present set of models the first to systematically account for variability in C-stars. We examine periods and growth rates in the models, and find that, while the fundamental mode is affected by the structure of the envelope, overtones are less sensitive to the interior and largely determined by the global properties. In the models, the frequency of the overtone with the largest degree of excitation is found to scale with the acoustic cut-off frequency at the stellar surface, a behaviour similar to that observed for the frequency of maximum oscillation power for solar-like oscillations in less evolved red giants. This allows us to provide a simple analytic prescription to predict the most-likely dominant mode as a function of stellar parameters. Best-fitting relations for periods are also provided. By applying results of pulsation models to evolutionary tracks, we present a general picture of the evolution of long-period variability during the TP-AGB, that we find consistent with observations. Models are made public through a dedicated web interface.

Key words: stars: AGB and post-AGB – stars: oscillations – stars: variables: general.

1 INTRODUCTION

The thermally pulsing asymptotic giant branch (TP-AGB) is the final stage in the evolution of low- and intermediate-mass stars. Among the plethora of complex processes involved in this evolutionary phase, stellar pulsation is one of the most interesting. Not only it is intimately interconnected with poorly understood processes such as dust formation and mass loss (see e.g. the recent review by Höfner & Olofsson 2018), but it is also an extremely valuable observable for the calibration of theoretical models and the estimate of global stellar parameters, since pulsation periods are strongly linked to stellar mass, radius, and effective temperature. Owing to their large radii, these stars exhibit variability characterized by periods of order of hundreds of days, hence the name of long-period variables (LPVs). The brightest and largest amplitude ones, the Mira variables, are observable at large distances, especially at infrared wavelengths. In that spectral range, they follow a clear period–luminosity (PL) relation, which makes them very promising distance indicators (Whitelock et al. 2013; Whitelock & Feast 2014; Menzies, Whitelock & Feast 2015; Yuan et al. 2017; Huang et al. 2018). The discovery of several other PL sequences in the LPV population of the Large Magellanic Cloud (LMC, Wood et al. 1999; see also Wood 2000; Soszyński et al. 2009; Wood 2015; Trabucchi et al. 2017), re-ignited interest in such stars. The additional sequences are populated by Semi-regular variables (SRVs) as well as OGLE Small Amplitude Red Giants (OSARGs; Wray, Eyer & Paczyński 2004; Soszyński et al. 2004), a relatively recent variability type associated with both red giant branch (RGB) and AGB stars, that make up for the majority of LPVs. SRVs and OSARGs oscillate (often simultaneously) in multiple low-order radial and non-radial modes (Soszyński et al. 2004), characterized by dis-

---

★ E-mail: michele.trabucchi@unipd.it

Published by Oxford University Press on behalf of the Royal Astronomical Society

tinct periods and excitation properties which depend on the stellar parameters of the evolutionary stage. They also have interesting properties which can be used for distance measurements (Rau et al. 2018). Overall, LPVs span several orders of magnitudes in each of luminosity (from $\sim 10^2$ to $\sim 10^5\,\mathrm{L}_\odot$), period (from a few days to a few thousands days) and amplitude (from $\sim 10^{-3}$ mag to several magnitudes), reflecting the dramatic changes in the structure of red giants during their late evolution. Their observed periods and amplitudes provide additional constraints, together with other observables, to be matched by models, allowing us to refine our knowledge of stellar structure and evolution.

Currently, the interpretation of LPVs in the framework of evolutionary models often relies on analytic prescriptions derived from restricted grids of pulsation models (e.g. Fox & Wood 1982; Wood, Bessell & Fox 1983; Ostlie & Cox 1986; Wood 1990), whereas updated models of luminous red giant variables have long been missing from the scientific literature, and a set of models systematically accounting for the full variety of TP-AGB stars has never been published.

Some recent advancement in this field include the work by Xiong, Deng & Zhang (2018) (see also Xiong & Deng 2007, 2013), who addressed the study of pulsation stability in red giants using a theory of non-local, time-dependent convection, and the promising results of 3D radiation-hydrodynamic models of Freytag, Liljegren & Höfner (2017, and references therein). However, the time-consuming nature of such models makes them unsuitable for the construction of large grids.

A critical shortcoming of previous models, with the exception of a few selected studies, is that they do not account for surface chemical enrichment expected in the TP-AGB phase. C-type stars, produced by the dredge-up of carbon, have characteristic spectral features that are dramatically different from those of their O-rich counterparts. This is a consequence of altered molecular equilibria, and the corresponding drastic change in the main sources of molecular opacity. Since atmospheric opacities affect stellar radii, it is reasonable to expect pulsation periods to be affected as well. Yet, whether C-rich and O-rich LPVs follow different PL relations has never been thoroughly addressed theoretically. Also, the dependence of PL relations upon metallicity is poorly studied from a theoretical point of view, despite the metallicity dependence being crucial for the calibration of PL relations as standard candles.

In this work, we present a new, large grid of linear, radial, non-adiabatic pulsation models of luminous red giants, with updated opacity data for CNO-varied metal mixtures. It was designed to widely cover the space of stellar parameters characterizing the AGB evolution in terms of total mass, core mass, luminosity, effective temperature, and chemical composition. Models include periods and amplitude growth rates for five radial pulsation modes, from the fundamental to the fourth overtone. Growth rates allow us to predict stability/instability of individual modes, and are used as a proxy of the expected observability. We use results from these models to discuss the evolution and properties of pulsation in LPVs.

This paper is structured as follows. In Section 2, we describe the relevant aspects in the modelling of static envelopes and the grid coverage of stellar parameters. We then discuss the stability analysis of the envelopes and their pulsation properties. In Sections 3 and 4, we make use of selected models in the grid to present a simplified picture of the evolution of LPVs in terms of pulsational stability and of oscillation periods. We expand the analysis to evolutionary tracks in Section 5, while Section 6 is dedicated to a summary and to conclusions.

2 MODELS AND METHODS

The grid of pulsation models presented here was constructed with the codes described in Wood & Olivier (2014), based on those presented in Fox & Wood (1982). The computation involves two steps: (1) the construction of a spherically symmetric, static envelope (Section 2.1), and (2) the linear stability analysis of its structure (Section 2.4).

2.1 Static envelope models

We computed spherically symmetric, static envelope models covering the range of stellar parameters necessary to study and interpret the observed pulsation properties of TP-AGB stars.

The computation of a static model is limited to the outer envelope (the layers above the H-burning shell). This simplifying assumption is justified by the fact that the stellar core and the envelope are effectively decoupled from a dynamical point of view, so that radial pulsation is essentially an envelope process. The value of the core mass, provided as an inner boundary condition, is computed from a core mass–luminosity relation derived from evolutionary models, while the core radius is kept fixed at $R_\mathrm{c} = 0.15\,\mathrm{R}_\odot$ as its effect on pulsation is negligible for the models considered here (see Section 2.3.3). Additional boundary conditions include the values of total (current) mass, luminosity, and chemical composition. The latter is defined by the metallicity (Z) and by the mass fractions of hydrogen (X), helium (Y), carbon (X_C), nitrogen (X_N), and oxygen (X_O). Convective energy transport is described by means of the mixing length theory (Cox & Giuli 1968) in both static and perturbed models.

2.2 Opacity data

Third dredge-up events are able to produce significant changes in the surface composition of TP-AGB stars (see e.g. Lattanzio & Wood 2003). When sufficient amounts of carbon produced by nuclear reactions in the interior are mixed into the envelope, the abundance of carbon by number can exceed that of oxygen, initially larger, leading to the formation of carbon stars. This is usually described in terms of the number ratio C/O of carbon and oxygen atoms at the surface.

The low effective temperature of TP-AGB stars favours the formation of molecules, and the CO molecule, due to its high binding energy, effectively locks all atoms of the least abundant of the elements C and O. All the remaining atoms of the most abundant of those two elements can then form other molecules. Therefore, molecular equilibria exhibit an abrupt change in the vicinity of the transition at C/O ~ 1, which is mirrored by a drastic alteration of the main sources of molecular opacity. This is very evident in the spectral energy distribution of O-rich stars, dominated by absorption bands of TiO, VO, and H_2O, while C-rich star exhibit strong absorption features of carbon-bearing molecules such as C_2, CN, and SiC.

At a given stellar luminosity, larger atmospheric opacities correspond to lower effective temperatures and larger radii, i.e. lower mean densities. Since pulsation periods depend on the mean density $\bar{\rho}$ of the envelope, it is clear that chemically consistent opacity data are necessary for the appropriate modelling of C-rich variable stars. For this reason, we employed detailed atomic and molecular opacities computed with the ÆSOPUS code (Marigo & Aringer 2009) in the pulsation models. Such Rosseland mean opacities are appropriate to describe the low-temperature range corresponding to

Table 1. Parameters and nodes defining the structure of the grid.

Parameter	Nodes				
$M/\mathrm{M}_{\odot}$	[0.6, 1.0] (step: 0.05), [1.0, 2.0] (step: 0.1) and [2.0, 7.0] (step: 0.2)				
$\log\,(L/\mathrm{L}_{\odot})$	[2.5, 5.0], step: 0.01 (boundaries depend on M, see Section 2.3.2)				
$M_{\mathrm{c}}/\mathrm{M}_{\odot}$	Defined as a function of luminosity (see equation 5 and Table 2)				
α_{ML}		1.5,	2.0,	2.5	
Z_{ref}	0.001,	0.002, 0.01,	0.004, 0.014,	0.006, 0.017	0.008,
X		0.6,	0.7,	0.8	
C/O	0.3, 1.05,	0.55, 1.3,	0.7, 1.8,	0.95, 3.0,	1.0, 5.0
$f_{\mathrm{C/O}}$	− 0.263, 0.281,	0.0, 0.374,	0.105, 0.515,	0.238, 0.737,	0.260, 0.959

the outer layers of the envelope ($3.2 \le \log\,(T[\mathrm{K}]) \le 4.5$). For the high-temperature regime (i.e. the stellar interior), we used the data from the Opacity Project (OP, Seaton 2005), covering the range $3.5 \le \log\,(T[\mathrm{K}]) \le 8.0$. For each combination of metallicity, hydrogen abundance, and C/O ratio (see Table 1 and Section 2.3.1), we computed two tables of opacity as a function of temperature and density, one with ÆSOPUS and the other with the OP routines. Each pair of tables was then smoothly merged in the overlapping temperature range.

2.3 Coverage of stellar parameters

We constructed the grid of pulsation models by varying several input parameters for the computation of static envelope models. To select the relevant parameters to be varied, as well as the corresponding range and sampling, we made use of detailed TP-AGB evolutionary tracks computed with the COLIBRI code (Marigo et al. 2013, 2017). The grid coverage is summarized in Table 1.

2.3.1 Chemical composition

In the computation of the present models, we take as reference the solar composition by Caffau et al. (2011). First, we computed a set of envelope models of scaled-solar composition, with metallicity Z from 0.001 to 0.017, and hydrogen mass fraction X: 0.6, 0.7, and 0.8. For each combination of X and Z, we then computed models with altered carbon abundance, described by the carbon variation factor[1] (see also Marigo & Aringer 2009) defined as

$$f_{\mathrm{C/O}} = \log\left(\frac{\mathrm{C}}{\mathrm{O}}\right) - \log\left(\frac{\mathrm{C}}{\mathrm{O}}\right)_{\mathrm{ref.}}, \qquad (1)$$

where C and O are the abundances by number of carbon and oxygen, respectively, and $(\mathrm{C/O})_{\mathrm{ref.}} = (\mathrm{C/O})_{\odot} = 0.54954$, or alternatively

$$f_{\mathrm{C/O}} = \log\left(\frac{Y_{\mathrm{C}}}{Y_{\mathrm{O}}}\right) - \log\left(\frac{Y_{\mathrm{C}}}{Y_{\mathrm{O}}}\right)_{\mathrm{ref.}}, \qquad (2)$$

where $Y_{\mathrm{C}} = X_{\mathrm{C}}/A_{\mathrm{C}}$, $Y_{\mathrm{O}} = X_{\mathrm{O}}/A_{\mathrm{O}}$, X_{C}, and X_{O} are the abundances of carbon and oxygen by mass fraction, and A_{C} and A_{O} are the corresponding mass numbers. The grid ranges from $f_{\mathrm{C/O}} = -0.263$ to 0.959, corresponding to C/O ratios from 0.3 (sub-solar) to 5.0 (see Table 1). Note that, with the exception of the scaled-solar case ($f_{\mathrm{C/O}} = 0$, $\mathrm{C/O} = (\mathrm{C/O})_{\odot}$), metallicity is not preserved when altering the abundance of carbon. For this reason, it is useful to identify models in terms of their 'reference metallicity' Z_{ref}, i.e. the metallicity they would have if no carbon variation was applied. The reference metallicity can be thought as that at the beginning of the AGB, i.e. prior to any third dredge-up event (see also Appendix A1).

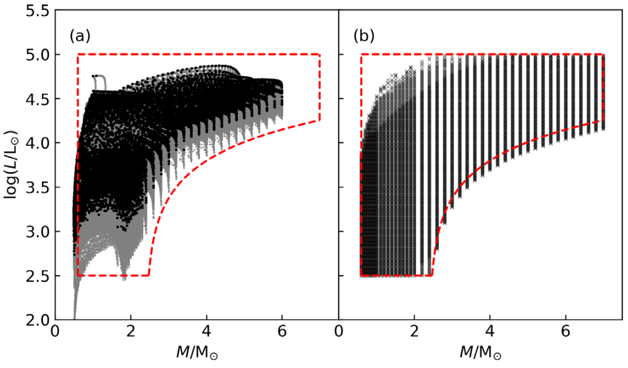

Figure 1. TP-AGB evolutionary models from COLIBRI (left-hand panel) and pulsation models from this work (right-hand panel) in the mass–luminosity plane. Evolutionary tracks including full thermal pulse cycles (TPCs) are plotted in grey colour, while black symbols represent quiescent points only (when the He-burning shell is dormant and energy is produced by the H-burning shell in quiet conditions). Dashed contours in both panels represent the nominal coverage of the grid. In some cases, the starting luminosity for a series of models was set slightly below that defined by equation (4) in order to facilitate calculations. As a result, models go below the nominal coverage in the higher mass range of the diagram.

We performed test calculations, over a limited portion of the space of parameters, in which variations of C/O have been obtained by changing the individual abundances of carbon and/or oxygen. The results suggest that the abundances of C and O, individually, have a minor effect on pulsation properties, while it is really C/O which plays a significant role.

Therefore, the assumption was made that variations of C/O are entirely due to changes in the amount of carbon, with oxygen abundance being always kept fixed to the scaled-solar value. The effect of changing the envelope abundance of oxygen, as well as an expansion of the metallicity range, will be addressed in a future version of the present grid of models.

2.3.2 Mass and luminosity

We computed pulsation models with masses in the range $0.6 \le M/\mathrm{M}_{\odot} \le 7.0$. Note that such values represent the current mass, and not the initial one. TP-AGB stars cover several orders of magnitudes of bolometric luminosity. Our models can have a luminosity in the interval $2.5 \le \log\,(L/\mathrm{L}_{\odot}) \le 5.0$ (Fig. 1), the actual range depending on mass, and to a minor extent on other input parameters. This interval covers the whole AGB, and includes the brightest part of the RGB.

To account for the fact that the more massive stars begin the TP-AGB phase at a higher luminosity, we set the lower luminosity limit L_{low} as a function of mass, according to the following expression

---

[1] Logarithms are to base 10 throughout this paper.

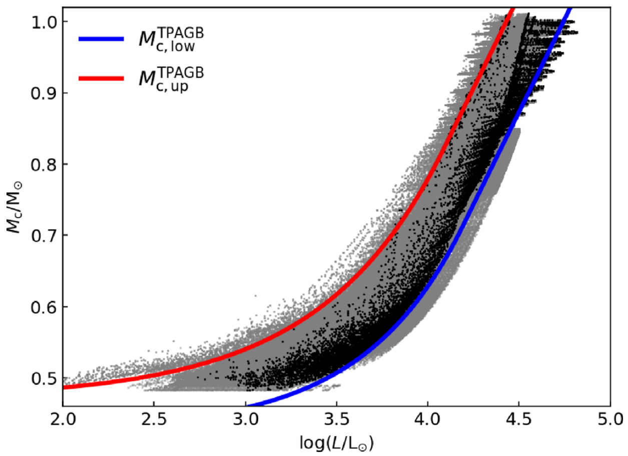

Figure 2. TP-AGB evolutionary models, computed with the COLIBRI code, in the core mass–luminosity plane. Grey dots in the background represent models including full TPCs, whereas black dots are quiescent phases. Solid lines represent the analytic relations for the upper (red) and lower (blue) limits of the region occupied by models.

derived from an inspection of evolutionary tracks:

$$\frac{L_{\rm low}}{{\rm L}_\odot} = \max\left(10^{2.5}, L_0(M)\right) \tag{3}$$

$$L_0(M) = 3882\frac{M}{{\rm M}_\odot} - 9294. \tag{4}$$

For computational reasons, the calculation of pulsation models is sequential in luminosity: the first model is computed with a luminosity given by equation (3), then additional models are computed by increasing the total luminosity by a step $\Delta\log(L/{\rm L}_\odot) = 0.01$, thus constructing a series of models having the same mass, chemical composition, and input physics, but differing in luminosity and core mass (see Section 2.3.3). Such a sequence is terminated at a fixed upper luminosity limit, $L = 10^5\,{\rm L}_\odot$, or at the luminosity where convergence failure arises. In either case, the resulting coverage is compatible with that expected from evolutionary calculations (Fig. 1). We stress that such luminosity sequences, used in the following sections to examine the development of variability in AGB models, are not evolutionary tracks, and should not be regarded as such.

2.3.3 *Core mass and radius*

It is well known that the total luminosity of AGB stars is largely determined by the core mass, a property usually known as 'core mass–luminosity relation' (CMLR). However, the classical CMLR breaks down in a number of cases, most notably during the luminosity dip associated with an He-shell flash, or in stars undergoing hot-bottom burning (HBB). As a result, evolutionary models do not follow a tight relation in the $M_{\rm c}$–$\log(L)$ plane, but are rather distributed in a broad stripe (Fig. 2). To account for this, instead of limiting the computation of envelope models to a single value of core mass (i.e. a single CMLR), we sampled the core mass–luminosity plane and derived two analytic CMLR representative, respectively, of the lower and upper limit values of core mass. To do so, we made use of COLIBRI TP-AGB evolutionary tracks (Marigo et al. 2017), and found that both the lower limit ($M_{\rm c,low}^{\rm TPAGB}(L)$) and upper limit ($M_{\rm c,up}^{\rm TPAGB}(L)$) relations are well described by a function of L that is

Table 2. Coefficients of the functions describing the upper ($M_{\rm c,up}^{\rm TPAGB}$) and lower ($M_{\rm c,low}^{\rm TPAGB}$) boundaries of the region populated by TP-AGB evolutionary models in the $M_{\rm c}$–$\log(L)$ plane. See also Fig. 2.

	$M_{\rm c,low}^{\rm TPAGB}$	$M_{\rm c,up}^{\rm TPAGB}$
ℓ	4.19	4.08
a_1	0.425	0.4708
a_2	9.425×10^{-6}	2.293×10^{-3}
a_3	0.7884	0.6468
a_4	1.4964	− 0.7103
b_1	− 1.52	− 1.279
b_2	0.5202	0.5202
b_3	0.1	− 0.05

linear at low luminosities and logarithmic at large luminosities. The adopted functional form is given by

$$\frac{M_{\rm c}}{{\rm M}_\odot} = \begin{cases} a_1 + a_2\cdot 10^{a_3\cdot[\log(L/{\rm L}_\odot)+a_4]} & \text{if } \log(L/{\rm L}_\odot) < \ell \\ b_1 + b_2\cdot\left[\log(L/{\rm L}_\odot) + b_3\right] & \text{if } \log(L/{\rm L}_\odot) \geq \ell \end{cases}, \tag{5}$$

with coefficients given in Table 2.

For each combination of the other grid parameters, we computed two envelope models, one for each of the two CMLRs. This approach represents a significant improvement with respect to the use of a single CMLR, in that the pulsation properties can be estimated for arbitrary values of core mass (for instance by interpolating in the two $M_{\rm c}$ values provided), thus allowing a more accurate coverage of the properties of TP-AGB stars. To test this approach, we have computed envelope models with values of core mass and luminosity that sample the whole region between the two CMLRs defined above, and extending substantially below the 'lower limit' CMLR. We examined the linear stability for those envelope models and found that periods $\log(P_n)$ and growth rates GR depend weakly on the core mass, and that the dependence is very close to linear. The interpolation and extrapolation of periods and growth rates as a function of core mass can thus be considered safe.

The core radius, on the other hand, has been kept fixed to a constant value $R_{\rm c} = 0.15\,{\rm R}_\odot$, that is a bit larger than the radius of the core (and of the H-burning shell) during most of the TP-AGB evolution. This choice implies the rather strong assumption that pulsation properties are at most weakly dependent upon the core radius. We verified that if the radius is instead obtained from a mass–radius relation for white dwarfs (physically more appropriate), there is no appreciable difference in the resulting periods and growth rates.

2.3.4 *Effective temperature*

The effective temperature is an output parameter from the integration of a static envelope model, and is essentially determined by the choice of the mixing length parameter $\alpha_{\rm ML}$. In evolutionary models, the mixing length parameter is calibrated by reproducing the observed properties of the present Sun. Envelope models such as the one used here are not coupled to any evolutionary calculation, so this procedure is not possible. Instead, $\alpha_{\rm ML}$ is usually tuned to reproduce some reference value of the effective temperature. For instance, in their modelling of LPVs in globular clusters, Lebzelter & Wood (2007, 2016) calibrated the mixing length parameter to reproduce the slope of the observed giant branch, obtaining values of $\alpha_{\rm ML}$ in the range ∼1.7 to ∼2.2. When computing envelope models with the requirement of reproducing the effective temperatures of COLIBRI models, we found a range of $\alpha_{\rm ML}$ consistent with those values.[2]

Therefore, we computed each pulsation model with three different values of the mixing length parameter: $\alpha_{\rm ML} = 1.5$, 2.0, and 2.5. As a result, pulsation models in the grid, for a given combination of mass, core mass, luminosity, and chemical composition, span a finite range of effective temperatures (using $\alpha_{\rm ML} = 2.5$ will result in a ∼15–20 per cent change in effective temperature, depending on other input parameters, with respect to the case in which $\alpha_{\rm ML} = 1.5$ is used). The major advantage of this is that pulsation models presented here can be used to estimate pulsation properties from the global parameters of any stellar model, regardless of the code it originates from and the corresponding calibration of $\alpha_{\rm ML}$.

2.4 Pulsation models

For each envelope model in the grid, we computed pulsation properties by performing linear stability analysis with the code described in Wood & Olivier (2014). As for the envelope models, convection is described by the mixing length theory (Cox & Giuli 1968). The interaction between convection and pulsation is treated in the simplified manner described in Fox & Wood (1982) based on the formalism by Arnett (1969), while models do not include turbulent pressure or the kinetic energy of turbulent motions. Turbulent viscosity, described in the pulsation code in terms of a free parameter α_ν (see Wood & Olivier 2014; Keller & Wood 2006, for more details), is sometimes included in non-linear calculations to bring predicted pulsation amplitudes in agreement with observations (see e.g. Ireland, Scholz & Wood 2008), and contributes to the damping of oscillations in linear pulsation models. However, since the turbulent viscosity parameter lacks a proper calibration as a function of global stellar parameters, we set $\alpha_\nu = 0$ in all models.

The result of the stability analysis applied to an envelope model consists of a set of complex eigenfrequencies. The number of pulsation modes to be searched is user-defined, and in this work we computed five modes for each model. Modes are identified by their radial order n, with $n = 0$ corresponding to the fundamental mode, $n = 1$ to the first overtone (1O) mode, $n = 2$ to the second overtone (2O) mode, and so on. The time dependence of the perturbations is assumed to be in the form $\xi \propto \exp(\omega t)$, with eigenfrequency $\omega = \omega_{\rm R} + \mathbf{i}\omega_{\rm I}$. The imaginary part of ω is the angular frequency of oscillation, and the period of the nth mode is defined as:

$$P_n = \frac{2\pi}{\omega_{{\rm I},n}}. \qquad (6)$$

While it is generally accepted that all red giants are variable to some extent (e.g. Percy, Wilson & Henry 2001, and references therein), not all of them exhibit photometric variations to a detectable level. Whether or not an oscillating star can be observed as variable depends on the photometric amplitude of its variability, as well as on the instrumental setup. In multiperiodic variables, the amplitude of a given mode with respect to the others is also important. In fact, LPVs are often characterized in terms of the observed properties of the dominant (or primary) mode, the one with the largest amplitude.

Since linear models are not able to predict pulsation amplitudes, we rely on a different approach to allow for the comparison with observations. The amplitude of a pulsation mode depends upon its degree of excitation, which is described by the non-adiabatic term of the eigenfrequency, i.e. the real part $\omega_{\rm R}$ (also known as stability coefficient). It is proportional to the inverse time-scale of exponential decay/amplification of the perturbation. A mode with $\omega_{\rm R} < 0$ is stable, and hence we expect that it is not observable, whereas an unstable mode has $\omega_{\rm R} > 0$, and it should be observable provided it has had the time to grow to a large enough amplitude. This latter condition corresponds to the requirement that $\omega_{\rm R}$ is larger than some (properly calibrated) threshold. In the following, we will use the amplitude growth rate,

$$\mathrm{GR}_n = \exp\left(2\pi\frac{\omega_{{\rm R},n}}{\omega_{{\rm I},n}}\right) - 1, \qquad (7)$$

as a proxy for excitation. This quantity describes the fractional rate of change in the radial amplitude per pulsation cycle (see also Fox & Wood 1982; Wood & Olivier 2014). This choice is justified by the findings of Trabucchi et al. (2017), who used some of the models presented here to study the population of LPVs in the LMC, and found that (1) growth rates are able to account for the observed instability strip, and (2) observed variability amplitudes scale with the predicted growth rates. The relation between the growth rate and the stability coefficient is further discussed in Section 3. We will assume hereafter that the dominant pulsation mode in a given envelope model corresponds to the one with the largest growth rate. It is important to keep in mind that, while the results of Trabucchi et al. (2017) are encouraging in this respect, growth rates depend on the treatment of poorly understood processes such as convection and its coupling with pulsation, and are therefore affected by uncertainties.

A significant fraction of the LPVs in the Milky Way and in the Magellanic Clouds with *I*-band magnitude fainter than the tip of the red giant branch (TRGB) have been recognized as RGB stars (see e.g. Ita et al. 2002, 2004; Kiss & Bedding 2003; Soszyński et al. 2004). As explained in previous sections, some of the parameter domains of the present grid have been defined using as reference TP-AGB models. We examine here whether the grid coverage is also appropriate for the global parameters of RGB stars down to ∼1 mag below the TRGB. Based on data from the third phase of the Optical Gravitational Lensing Experiment (OGLE-III, Soszyński et al. 2009), that limit would correspond to $K_{\rm s} \simeq 14$ mag, or $\log(L/{\rm L}_\odot) \gtrsim 2.5$, meaning that our grid coverage is sufficient to describe OSARGs in the RGB phase.

At a given luminosity, the main differences between RGB and AGB stars in terms of global parameters are effective temperature, mass, and core mass. The mass coverage in the grid ($0.6 \le M/{\rm M}_\odot \le 7.0$) is safely appropriate for RGB stars in the regime of interest for long-period variability, and the three nodes of $\alpha_{\rm ML}$ used in constructing the grid cover a wide enough range of temperatures to account for the slightly colder RGB stars. On the other hand, the core mass in RGB stars is smaller with respect to AGBs at the same luminosity, and actually falls below the 'lower limit' CMLR discussed in Section 2.3.3. In other words, the use of our models to predict pulsation properties of RGB stars, e.g. by interpolation in the grid (see Appendix A1) will result in extrapolation below the lower $M_{\rm c}$ boundary of the grid. However, for low $M_{\rm c}/M$ ratios, predicted periods and growth rates of radial modes appear to depend weakly on the core mass. Moreover, the dependence is very close to linear, suggesting that even when extrapolating towards lower masses one would obtain values close to those resulting from direct calculations (see Section 2.3.3). According to these arguments, the grid coverage is appropriate for the global parameters of RGB-OSARGs.

---

[2] Differences in $T_{\rm eff}$ between envelope and evolutionary models when using the same value of $\alpha_{\rm ML}$ are primarily due to the different input physics and boundary conditions employed in the two codes.

Finally, it should be kept in mind that these considerations are only valid under the assumption that the core is dynamically decoupled from the envelope, an approximation that is generally valid also for luminous RGB stars.

Note also that Trabucchi et al. (2017) used some of the models presented here to study both the AGB and the RGB populations of LPVs in the LMC, obtaining reasonably good agreement with observations. We therefore consider our models suitable enough to study radial oscillations in bright RGB stars, provided the arguments above are taken into account in the interpretation of the results.

The results of the models are collected in tables giving global stellar parameters, together with the adiabatic frequency and the real and imaginary parts of the non-adiabatic frequency for five radial modes, from the fundamental to the 4O mode. Table 3 shows a typical output as an example, displaying frequencies for the fundamental, 1O, and 2O modes.

3 PULSATIONAL STABILITY

In the present section, we examine the stability of pulsation in different radial modes, and how it depends upon global stellar parameters. To begin with, we consider a series of models of increasing radius and luminosity, and with fixed mass, composition, and input physics, i.e. one of the luminosity sequences of the grid. Values of the fixed quantities are summarized in Table 4, and are representative of typical O-rich TP-AGB variables in the LMC. Changing the other parameters does not alter significantly the picture provided here, except in the high-mass range of the grid. This is discussed in Section 3.2.

The behaviour of growth rates as a function of increasing luminosity allows us to present a general picture of the evolution of pulsational stability during the AGB. Compared to full evolutionary tracks, it provides us with a simplified framework, suitable for understanding the main factors determining the global evolution of LPVs. We complete this picture in Section 5, where periods and growth rates along proper evolutionary tracks are analysed.

Fig. 3 shows periods and growth rates for the five lowest order radial modes as a function of radius along the selected luminosity sequence. Given the dynamical nature of stellar pulsation, periods scale approximately as the free-fall time of the star (proportional to the inverse square root of the mean stellar density), and thus increase with radius approximately as a power law.

Growth rates GR show a more complex, characteristic pattern. At low radii, all modes have rather small (or even negative) growth rates, meaning that stars at this stage would exhibit only low-amplitude variability, or no detectable variability at all.[3] Growth rates increase with luminosity, following a trend that is qualitatively the same for all modes, with the exception of the fundamental mode. Overtone modes growth rates increase more or less steadily until they reach a peak-shaped maximum, after which they undergo a quick drop towards negative values. Note that after this stage, the growth rate never recovers to positive values: once an overtone mode has passed through its stage of maximum growth rate, it becomes definitively stable. In a real AGB star, this is true as long as the stellar radius grows with time: if, on the other hand, the star shrinks, e.g. after a thermal pulse, a stable overtone mode can become unstable again (see Section 5). The 1O mode represents an exception to this, as its growth rate usually keeps positive values even past the 'peak': in principle, it should be detectable with finite amplitude up to the highest luminosities.

Beginning from the low-luminosity end of a sequence, the highest radial order in our calculations, the 4O mode, is the first to reach the maximum, followed by the 3O, 2O, and 1O modes in this order. When a mode is approaching its point of maximum instability, its growth rate is larger than that of all other modes, and we tag it as 'dominant' (see the discussion in Section 3.3). In terms of the evolution of an LPV, this means that at low luminosity, the dominant mode is a relatively high-order overtone (probably the 3O mode, see Trabucchi et al. 2017). As the star evolves, that mode becomes stable, and the overtone of immediately lower order takes over as dominant. This event is repeated in a series of 'shifts' towards lower order modes, until eventually the fundamental mode becomes dominant, a well-known characteristic of red giant variables (see e.g. Lattanzio & Wood 2003; Xiong et al. 2018 and references therein).

The behaviour of the fundamental mode growth rate is clearly different, and is discussed in Section 3.1.

Overtone modes are essentially confined near the surface of the models, as displayed in the top panel of Fig. 4. Their properties are thus in large part determined by physical conditions in the outermost stellar layers. We make use of the partial work integral $W(r)$ (see e.g. Cox 1980; Fox & Wood 1982) to understand the driving of pulsation. $W(r)$ represents the amount of work done per unit time by all mass layers interior to a certain position r. Driving regions, where $W(r)$ increases outward, provide positive work, i.e. feed energy into pulsation motion. All the overtone modes have a significant amount of driving coming from the outer part of the partial hydrogen ionization zone. To examine what happens as models evolve, for each mode we consider both the growth rate and the stability coefficient $\omega_{\mathrm{R},\,n}$ the latter being proportional to the work integral. A clear difference between GR and ω_{R}, evident in Fig. 3, is that the former grows with increasing radius, while the latter is approximately constant. This means that the increasing instability (and amplitude) experienced by overtone modes is not due to an increase in the rate of work done, but rather to the fact that the amount of work is integrated over a longer pulsation period (compare with the definition of growth rate, equation 7).

This is true, at least, prior to the point of maximum growth rate, after which ω_{R} also drops to negative values. However, this abrupt stabilization is not due to driving processes: it is a purely mechanical effect determined by the choice of realistic boundary conditions in the pulsation models (described in Wood & Olivier 2014). The propagation of acoustic perturbations in the form of standing waves (i.e. pulsation modes) in a stellar envelope occurs only if their frequency is smaller than a critical value, the acoustic cut-off frequency ν_{ac}, determined by the surface properties of envelope models. When a mode's frequency exceeds ν_{ac}, pressure waves travelling towards the surface are not reflected back to the interior, but will rather propagate outward through the atmosphere, dissipating the pulsation energy and thus rendering the mode stable.

The regular stabilization pattern of overtone modes can be easily understood if we consider the expression of the acoustic cut-off frequency in the approximation of an isothermal atmosphere:

$$\nu_{\mathrm{ac}} = \frac{1}{4\pi} G \left(\frac{m_{\mathrm{H}}}{k_{\mathrm{B}}}\right)^{1/2} \left(\frac{\mu \Gamma_1}{T}\right)^{1/2} \frac{M}{R^2}, \tag{8}$$

where G is the gravitational constant, m_{H} is the atomic mass unit, k_{B} is the Boltzmann constant, μ is the mean molecular weight, $\Gamma_1 = (\mathrm{d}\ln P/\mathrm{d}\ln \rho)_{\mathrm{ad}}$ is the adiabatic exponent, M and R are the surface mass and radius, and $T \sim T_{\mathrm{eff}}$ is the surface temperature. While

---

[3] While the present models are limited to five radial modes, calculations including a larger number of modes have been carried out, and we did not find any mode to deviate from the picture given here.

Table 3. Example of results for a selected series of pulsation models. Defining parameters of the sequence are shown in the header. The complete set of tables is available for download from the website http://starkey.astro.unipd.it/web/guest/pulsation (see Appendix A).

$M = 1.5\,\mathrm{M}_\odot,\ \alpha_{\mathrm{ML}} = 2.0,\ \mathrm{CMLR} : M^{\mathrm{TPAGB}}_{\mathrm{c,low}}$
$Z_{\mathrm{ref}} = 0.006,\ X = 0.7,\ f_{\mathrm{C/O}} = 0.,\ \mathrm{C/O} = (\mathrm{C/O})_\odot = 0.54954$

log L/L$_\odot$	log T_{eff}/K	M_{c}/M$_\odot$	$\omega_{\mathrm{ad,\,0}}$	$\omega_{\mathrm{R,\,0}}$	$\omega_{\mathrm{I,\,0}}$	$\omega_{\mathrm{ad,\,1}}$	$\omega_{\mathrm{R,\,1}}$	$\omega_{\mathrm{I,\,1}}$	$\omega_{\mathrm{ad,\,2}}$	$\omega_{\mathrm{R,\,2}}$	$\omega_{\mathrm{I,\,2}}$
			(angular frequencies in μHz)								
	...			...			...			...	
3.70	3.551	0.543	0.4607	−0.0011	0.4628	0.8402	0.0143	0.8624	1.2944	−0.0082	1.3439
3.71	3.550	0.545	0.4453	−0.0011	0.4474	0.8176	0.0142	0.8396	1.2610	−0.0088	1.3110
3.72	3.549	0.547	0.4304	−0.0012	0.4323	0.7956	0.0142	0.8174	1.2284	−0.0093	1.2788
3.73	3.548	0.549	0.4159	−0.0012	0.4177	0.7742	0.0142	0.7958	1.1966	−0.0099	1.2476
3.74	3.546	0.552	0.4018	−0.0012	0.4035	0.7534	0.0142	0.7747	1.1656	−0.0104	1.2169
3.75	3.545	0.554	0.3880	−0.0012	0.3896	0.7331	0.0142	0.7543	1.1354	−0.0108	1.1871
3.76	3.544	0.556	0.3747	−0.0012	0.3761	0.7133	0.0142	0.7343	1.1058	−0.0113	1.1580
3.77	3.543	0.558	0.3616	−0.0012	0.3629	0.6939	0.0142	0.7146	1.0766	−0.0117	1.1293
3.78	3.542	0.561	0.3490	−0.0012	0.3502	0.6752	0.0142	0.6957	1.0485	−0.0123	1.1016
3.79	3.540	0.563	0.3368	−0.0011	0.3378	0.6570	0.0142	0.6773	1.0211	−0.0126	1.0747
3.80	3.539	0.566	0.3249	−0.0011	0.3257	0.6393	0.0142	0.6594	0.9943	−0.0130	1.0485
	...			...			...			...	

Table 4. Global parameters of the selected series of models discussed in Sections 3 and 4, and displayed in Fig. 3.

Parameter	Value
M/M$_\odot$	1.5
$Z\ (=Z_{\mathrm{ref}})$	0.006
X	0.7
C/O	$(\mathrm{C/O})_\odot \simeq 0.55$
α_{ML}	2.0
M_{c}	‘lower limit’ CMLR

$\nu_{\mathrm{ac}} \propto MR^{-2}$, the oscillation frequency of a given overtone mode of radial order n scales as $\nu_n = P_n^{-1} \sim M^{1/2}R^{-3/2}$. This means that both frequencies decrease as the star expands, but ν_{ac} does so at a faster rate, and eventually the two cross each other, as displayed in Fig. 3 (see also fig. 3, top panel, of Wood & Olivier 2014). Maxima of the growth rates occur exactly when $\nu_n = \nu_{\mathrm{ac}}$.

The abrupt stabilization of overtone modes that exceed the acoustic cut-off is the very reason for the right edges of the PL sequences of LPVs observed in the Magellanic Clouds (with the exception of sequence C associated with fundamental mode pulsation). As a consequence of this behaviour, overtone modes are dominant, and most easily observable, when their frequency is close to the acoustic cut-off value.

Remarkably, this behaviour is similar to that followed by solar-like oscillations in less luminous red giants. Solar-like oscillations are observed in main sequence and post-main sequence stars with a convective envelope and $T_{\mathrm{eff}} \lesssim 6500K$. Their oscillation spectra present radial and non-radial modes that are stochastically excited and damped by sub-photospheric convection.

Ultraprecise photometric observations by the space telescopes *CoRoT* (Baglin et al. 2009) and *Kepler* (Borucki et al. 2009, 2010) have allowed the characterization of the properties of solar-like spectra for evolutionary stages going from the main sequence to the evolved red giant region. The global properties of these spectra are defined by two parameters, ν_{max} and $\langle\Delta\nu\rangle$, that depend on global stellar properties (see e.g. Chaplin & Miglio 2013). The power spectrum consists in a set of regularly spaced radial and non-radial modes whose amplitudes appear modulated by a Gaussian-shape envelope centred at ν_{max} and full width at half-maximum (for red giants) given by $\sigma \simeq 0.28\,\nu_{\mathrm{max}}^{0.15}\,\langle\Delta\nu\rangle$ (Mosser et al. 2010). The frequency at maximum power, ν_{max}, appears to scale with the acoustic cut-off frequency (see Brown et al. 1991; Kjeldsen & Bedding 1995; Belkacem et al. 2011, and the recent improvement by Viani et al. (2017) that includes also the dependence on the mean molecular weight). The so-called large-frequency separation, $\langle\Delta\nu\rangle$, is the difference in frequency between modes with consecutive radial order and same angular degree, and, in the asymptotic regime, scales with $\bar{\rho}^{1/2}$ (the square root of stellar mean density, Ulrich 1986; Kjeldsen & Bedding 1995). Taking into account the asymptotic expression for the frequency of radial modes ($\nu_n = (n+\varepsilon)\langle\Delta\nu\rangle$, it is obvious that as a star of mass M evolves along the RGB the radial order of the mode corresponding to the maximum power (n_{max}) shifts to lower values as radius increases ($n_{\mathrm{max}} \propto (M/(R\,T_{\mathrm{eff}}))^{1/2}$). Moreover, the mean density is decreasing, and so is the frequency domain of the oscillation spectrum, leading to a smaller number of radial orders in the spectrum. The kind of ‘universal pattern’ shown by oscillations in red giants allowed Mosser et al. (2013) to link the most luminous variables observed by *Kepler* with LPVs in OGLE.

Low-order overtone modes in LPVs and high-luminosity solar-like pulsators on the RGB share the property of showing the largest amplitude for frequencies approaching to the cut-off value. Whether or not the excitation mechanism is the same for both kinds of pulsators is still matter of debate (e.g. Christensen-Dalsgaard, Kjeldsen & Mattei 2001; Dziembowski et al. 2001; Xiong & Deng 2013), and the fact above described should not be immediately interpreted as an evidence for a common excitation mechanism, but rather as an indication that properties of low-order radial modes are largely determined by global stellar properties (surface gravity and temperature).

3.1 Stability evolution of the fundamental mode

The evolution of the fundamental mode growth rate is intrinsically different from that of the overtone modes. It does not increase monotonically with radius, but rather shows an intermediate phase of decrease during which it reaches a minimum value (depending on mass, see Section 3.2). In models of intermediate mass ($1 \lesssim M/\mathrm{M}_\odot \lesssim 4$, depending on chemistry and input physics), the fundamental mode growth rate is negative at the minimum, implying stability. This stage is followed by a very steep increase, causing the linear growth rates of the fundamental mode to become extremely large

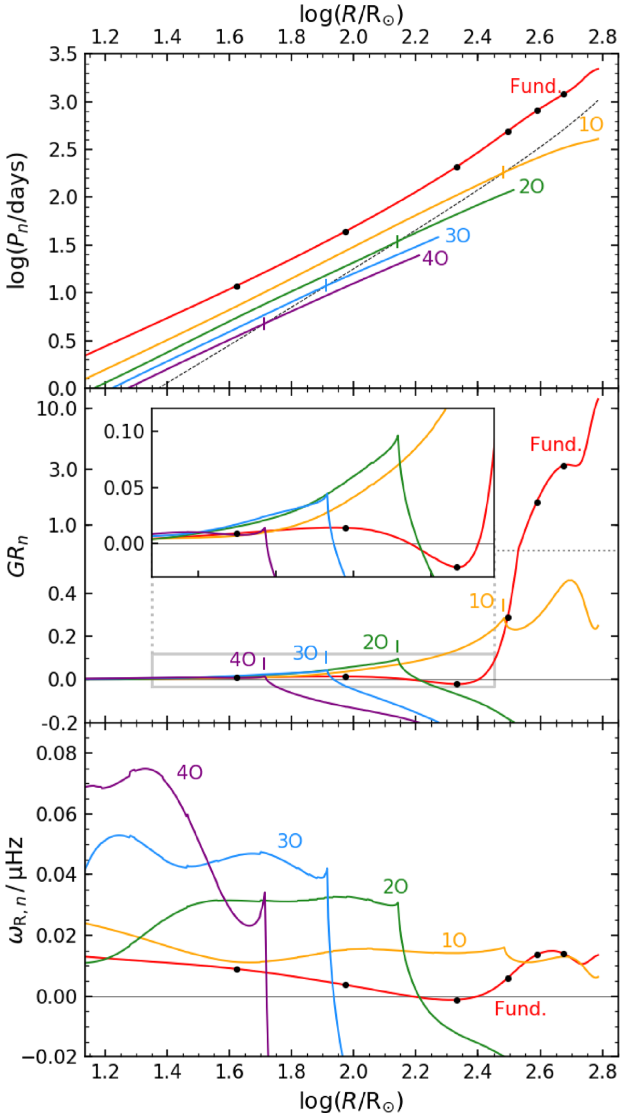

Figure 3. Global pulsation properties as a function of stellar radius for a selected series of models (see Table 4). Top panel: pulsation periods (solid lines) and the period corresponding to the acoustic cut-off (see Section 3). Middle panel: amplitude growth rates (equation 7); the inset shows an exploded view around GR = 0. Note that the vertical scale is linear below GR = 0.6, but becomes logarithmic above this value (dotted horizontal line) to better illustrate the rise of GR for the fundamental mode. Bottom panel: stability coefficients $\omega_{\mathrm{R},\,n}$. Vertical ticks mark the peaks of overtone modes growth rates in the top and middle panels. Black filled circles correspond to the selected models shown in Fig. 5.

($\mathrm{GR}_0 \gg 1$) at high luminosity. This would mean that pulsation amplitudes should increase by a factor of several at each pulsation cycle. This is clearly unrealistic from a physical point of view, and stems from the fact that the linear approximation for oscillations tends to break down at high luminosities. None the less, this result is qualitatively meaningful, and we interpret it as a phase of large-amplitude fundamental mode pulsation (in other words, the Mira-like phase).

In contrast with overtone modes, the (temporary) stabilization of the fundamental mode is not caused by its frequency reaching the acoustic cut-off. In fact, the present models suggest that the fundamental mode never reaches the cut-off (Fig. 3, top panel). Moreover,

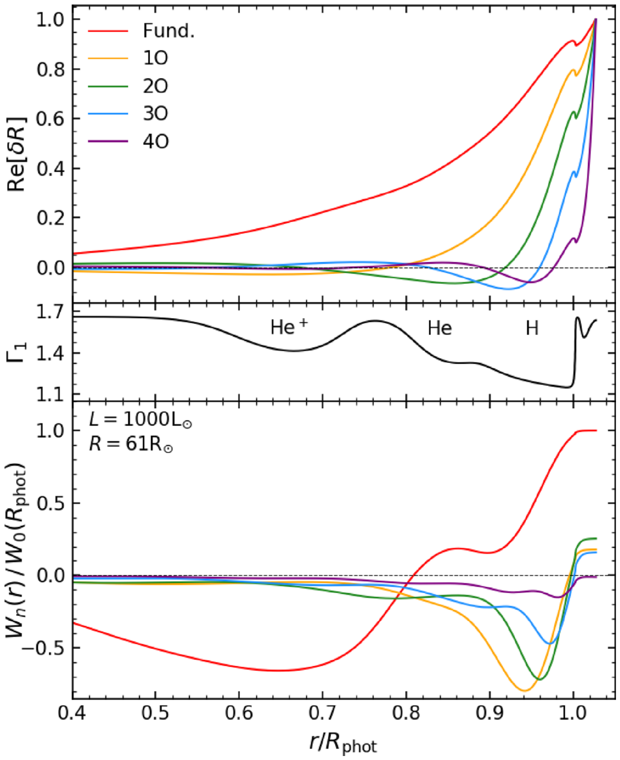

Figure 4. Internal pulsation properties for the model with $L = 1000\,\mathrm{L}_\odot$, $R = 61\,\mathrm{R}_\odot$ and belonging to the selected luminosity sequence (see Table 4). Radial displacement eigenfunctions and partial work integrals as a function of fractional radius are displayed in the top and bottom panels, respectively. To simplify the visual comparison, the partial work integrals are normalized to the surface value of the fundamental mode. The adiabatic exponent Γ_1 is shown in the middle panel, highlighting the regions of partial ionization and molecular dissociation of major elements. The interior amplitude of overtone modes is essentially zero everywhere except for the outer $\lesssim$10 per cent of the stellar radius, corresponding to the outer part of the H ionization zone. The 1O mode extends a bit deeper (but still with low interior amplitude) down to the first He ionization zone. The fundamental mode is the only one with significant interior amplitude in a large portion of the envelope, including all major ionization zones. Regions above ∼65 per cent of the radius contribute to driving the fundamental mode, while overtone driving regions are limited to the outer part of the H ionization zone.

the fundamental mode would reach the cut-off frequency at larger radii than the 1O mode, while the fundamental mode stabilization actually precedes the peak of the 1O mode's growth rate. It is thus clear that the fundamental mode growth rate is affected by actual non-adiabatic processes taking place within the envelope. A detailed investigation of the driving mechanism of the fundamental mode, with particular attention to the role of convection, is highly desirable to properly interpret the results of pulsation models. This kind of analysis, however, is beyond the scope of this work, and will be the subject of a forthcoming study. We limit the discussion here to the observation that the growth rate of the fundamental mode is strongly sensitive to the internal structure of the envelope, and in particular to the displacement of the region of ionization of major elements. This is displayed in Fig. 5, where the partial work integral $W(r)$ (solid red line) of the fundamental mode is shown for a few models along the selected luminosity sequence (marked by black filled circles in Fig. 3). It is worth pointing out that this property of the fundamental mode makes it difficult to relate either

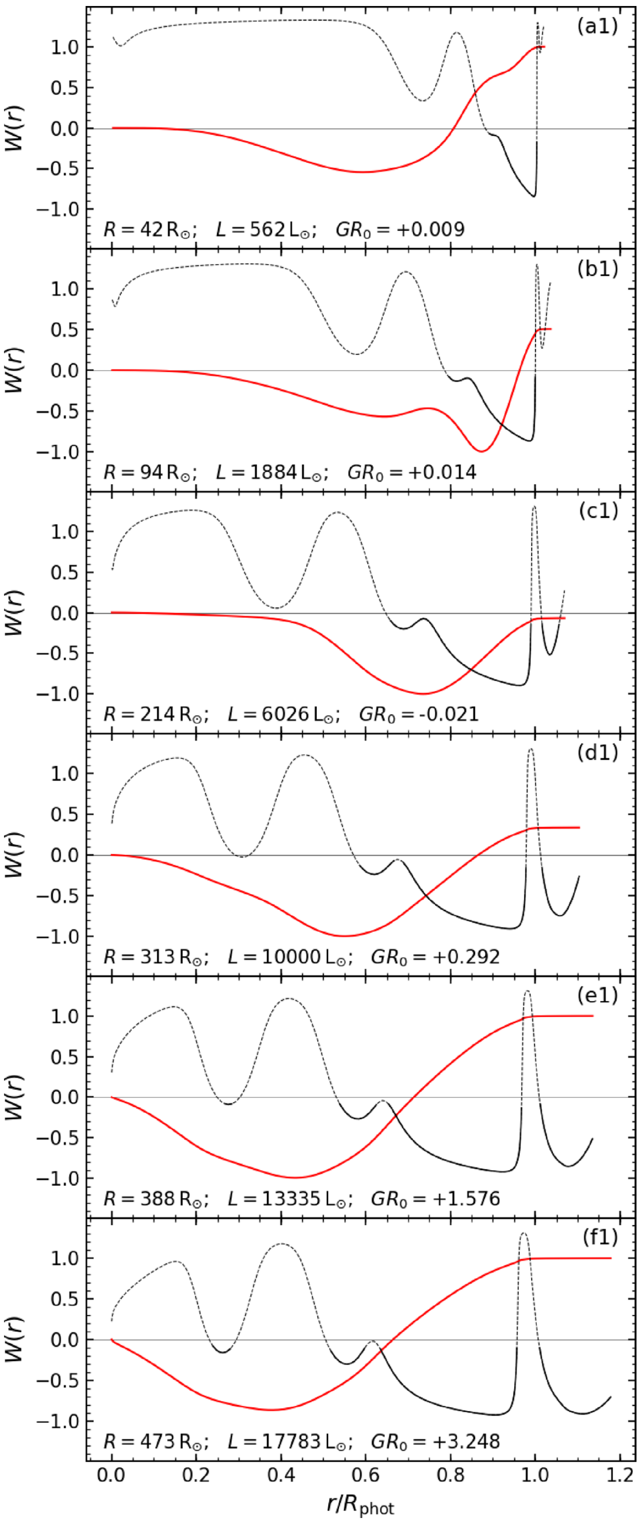

Figure 5. Partial work integral (normalized to the absolute maximum) of the fundamental mode for six models in the selected luminosity sequence (Table 4). The radial profile of the adiabatic exponent Γ_1 is also shown to highlight the location of partial ionization and molecular dissociation zones of major elements (dashed line, shown as solid line instead where $\Gamma_1 < 4/3$). Models shown here are marked by black filled circles in Figs 3 and 17. Luminosity increases from top to bottom panels.

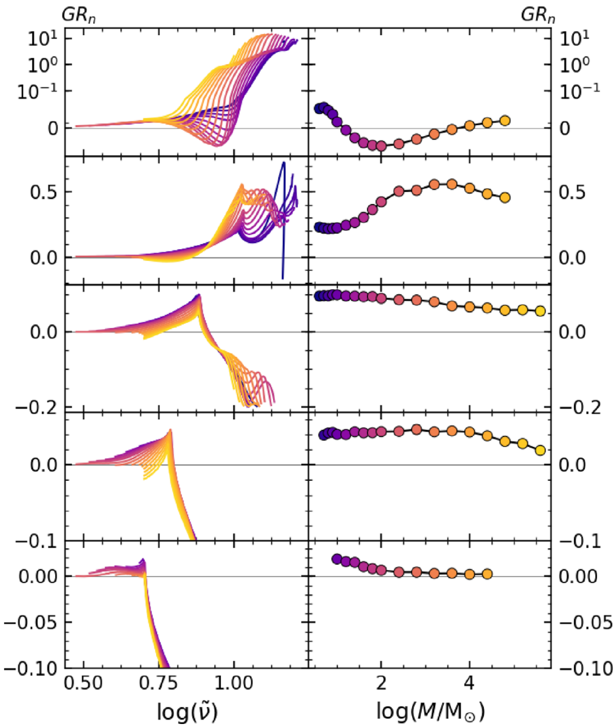

Figure 6. Left-hand panels: growth rates as a function of $\tilde{\nu}$ (see the text) for modes from the fundamental (top) to the 4O (bottom). Each line represents a series of models with a given mass, colour coded as in the right-hand panel. Global parameters other than mass are those summarized in Table 4. Right-hand panels: value $\mathrm{GR}_{\mathrm{max,n}}$ of the growth rate at the acoustic cut-off for each series of models, as a function of the corresponding mass. For the fundamental mode, the value of the growth rate at the minimum is shown instead.

its growth rate or its period to global stellar parameters in a simple and straightforward way (see also Section 4.3).

3.2 Dependence of growth rates upon stellar parameters

The discussion in the preceding sections is limited to the case of a specific mass, composition, and input physics. Here, we expand the discussion to different input parameters. Note that the total radius, used above as a proxy for the evolutionary status, is not convenient to compare the evolution of stability in models with significantly different global parameters. On the other hand, we have seen that the evolution of growth rates is determined by the values of the oscillation frequency with respect to the acoustic cut-off frequency. It is known from the theory of stellar pulsation (e.g. Cox 1980) that oscillation frequencies scale as $\nu \sim \bar{\rho}^{1/2}$, where $\bar{\rho} = 3M/4\pi R^3$ is the mean stellar density. Thus it is convenient to define the quantity

$$\tilde{\nu} = \left(\frac{M}{\mathrm{M}_\odot}\right)^{-1/2} \left(\frac{R}{\mathrm{R}_\odot}\right)^{1/2} \left(\frac{T_{\mathrm{eff}}}{\mathrm{T}_{\mathrm{eff},\odot}}\right)^{1/2} \propto \frac{\nu}{\nu_{\mathrm{ac}}}, \qquad (9)$$

to be used in place of the total radius in our analysis.

3.2.1 *Varying mass*

The advantage of this newly defined parameter becomes clear in Fig. 6, where growth rates are displayed as a function of $\tilde{\nu}$ for series of models with different masses. Note that $\tilde{\nu}$ increases as a star evolves to higher luminosities even though ν_n decreases. This is because ν_n decreases with advancing evolution less rapidly than $\nu_{\rm ac}$. It is clear that in Fig. 6, for a given overtone, growth rates reach the 'peak' at approximately the same value of $\tilde{\nu}$ for all masses, and the same is true for varying chemical composition and input physics. We are thus able to compare very easily the 'shape' of the growth rate evolution for models that are rather different from each other. For overtone modes higher than the 1O, the trend is almost the same for all masses, the major effect being a systematic (but small) decrease in growth rates towards the high masses. This is highlighted in the right-hand panels of Fig. 6, where the value $\mathrm{GR}_{\rm max,\,n}$ of the growth rate at the cut-off is displayed as a function of mass. For the 1O mode, growth rates are substantially larger towards higher masses, especially in the neighbourhood of the acoustic cut-off. On the other hand, at small values of $\tilde{\nu}$, more massive models have smaller growth rates, possibly negative.

Fig. 6 also shows the fundamental mode growth rates for which $\tilde{\nu}$ is less effective in providing a framework for comparison. The reason, as already discussed, is that overtone modes are largely determined by surface properties, encoded by $\nu_{\rm ac}$, while the fundamental mode is more sensitive to the envelope structure. The fundamental mode experiences temporary stabilization only for a limited interval of masses, $1.2 \lesssim M/\mathrm{M}_\odot \lesssim 3.5$. This is especially clear from the top right panel of Fig. 6, showing the value of $GR_{\rm min,\,0}$ (the fundamental mode growth rate at the local minimum) as a function of mass. Outside that range of masses, we find two possible trends: either the growth rates experience a positive minimum thus not becoming stable, or show an essentially monotonic increases with no minimum at all. The latter occurs for stars more massive than $\sim 4.5\,\mathrm{M}_\odot$. Note that the most massive models also show an earlier rise of the growth rate (at lower values of $\tilde{\nu}$ or L). A consequence of these trends is that, in the most massive models, it is possible for the fundamental mode to be excited and dominant over the whole luminosity interval of the grid. In that case, the regular pattern of shifts of the dominant mode towards lower radial orders, discussed in the previous sections, does not occur.

3.2.2 *Varying metallicity*

The effect of varying metallicity on the behaviour of growth rates is displayed in Fig. 7, and is essentially negligible for the 3O and 4O modes. The only relevant effect for the 2O mode occurs when it has already exceeded the acoustic cut-off, and is thus not relevant. On the other hand, we find the 1O mode growth rate at the cut-off to be significantly larger at low metallicity. This effect is even more pronounced at higher luminosities. This trend is found also for the fundamental mode, that, in the regime of temporary stabilization, shows larger growth rates for lower values of metallicity.

3.2.3 *Varying helium and hydrogen abundances*

Fig. 8 compares the evolution of growth rates for series of models with different values of the helium mass fraction, Y. Again, we find mild effects on the values of the growth rates of the 2O, 3O, and 4O modes, while the 1O mode shows larger values of $GR_{\rm max,\,1}$ for higher helium contents. Note, however, that this occurs as the more He-rich sequences reach the acoustic cut-off later (the peak of growth rates appears at larger $\tilde{\nu}$ for all overtones). This is a consequence of a higher value of the mean molecular weight term in equation (8), neglected in the definition of $\tilde{\nu}$ (equation 9). As for the

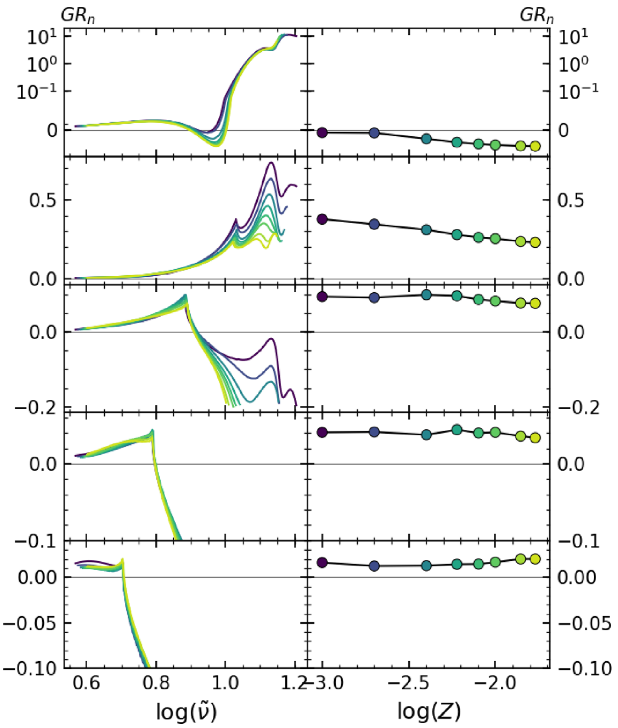

Figure 7. Same as Fig. 6, but showing series of models with different metallicity. Other global parameters are those summarized in Table 4.

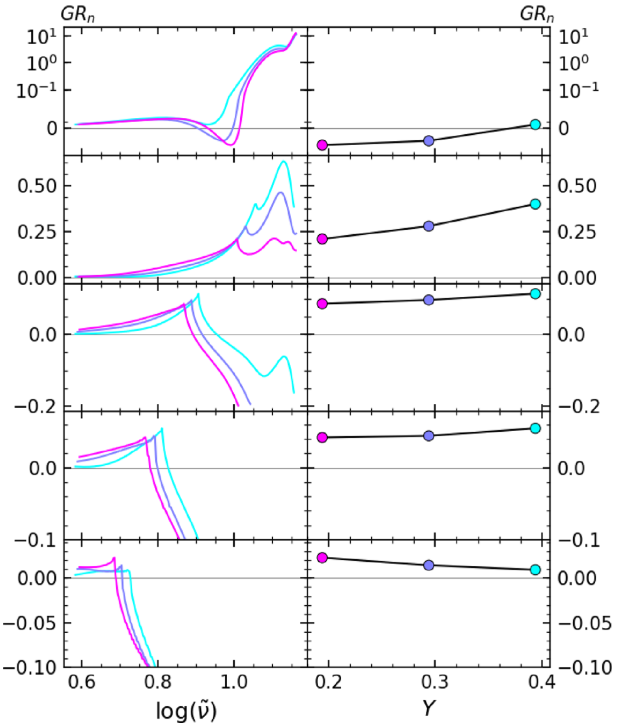

Figure 8. Same as Fig. 6, but showing series of models with different helium content. Other global parameters are those summarized in Table 4.

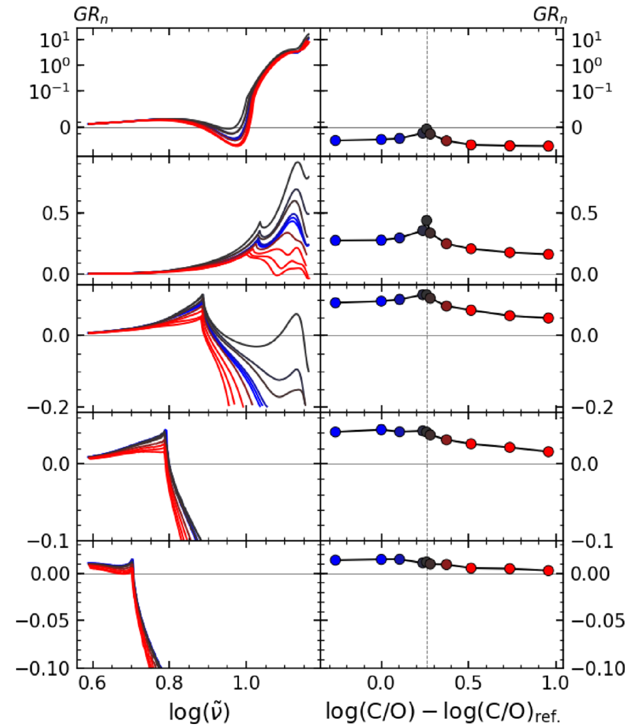

Figure 9. Same as Fig. 6, but showing series of models with different C/O. Other global parameters are those summarized in Table 4. Vertical dashed lines in the right-hand panels indicate C/O = 1.

fundamental mode, a higher abundance of helium adds a significant contribution to the driving, especially in the regime of temporary stabilization.

3.2.4 Varying C/O

The impact of an enhanced carbon abundance on growth rates is shown in Fig. 9. In the regime where overtone modes higher than the 2O are excited, the surface temperature of the models is too large for the formation of molecules to have any appreciable effect on pulsation. Thus, the decrease of $GR_{\mathrm{max,\,n}}$ towards higher C/O simply reflects the effect of an increased metallicity. For the 2O and 1O modes, stronger effects begin to be visible, with growth rates being enhanced in the vicinity of C/O $\simeq 1$. The same is true for the fundamental mode, in the neighbourhood of the point of minimum growth rate. Note that the growth rate peak of the 1O mode shows the same displacement discussed in the case of varying He abundance, though in this case, the cause is mostly the variation of the Γ_1 term in equation (8) rather than the mean molecular weight term.

3.2.5 Varying α_{ML}

The growth rates of low- and high-order modes show an opposite dependence upon the mixing length parameter (Fig. 10). The 3O and 4O modes suffer a significant reduction in growth rates when α_{ML} is increased, while the opposite is true for the 1O and fundamental mode. The 2O mode growth rate is remarkably insensitive to the value of α_{ML}, at least for the combination of mass and chemical composition considered here. Note that the effect on the fundamental mode growth rates resulting from increasing α_{ML} is somewhat similar to that produced by an increase in helium content.

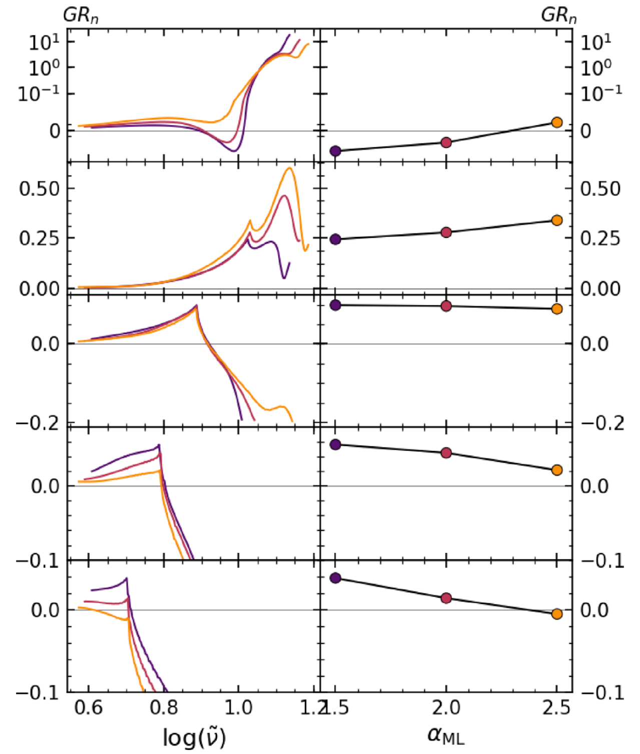

Figure 10. Same as Fig. 6, but showing series of models computed with a different value of the mixing length parameter α_{ML}. Other global parameters are those summarized in Table 4.

3.3 Analytic prescription for pulsational stability

The regularity shown by overtone modes growth rates allows us to construct a conveniently simple model to describe pulsational stability as a function of stellar parameters. To begin with, we recall that overtone modes become stable when the star evolves to the point where their frequency exceeds the acoustic cut-off value, determined by surface properties. Usually, this results in the exclusion of all overtone modes with a radial order larger than some value n_{d}. Among the remaining modes, the one with $n = n_{\mathrm{d}}$ has the shortest period, and very likely the largest growth rate, so we can expect it to be dominant. Modes with $n < n_{\mathrm{d}}$ are likely excited, the mode with $n = n_{\mathrm{d}} - 1$ having the second largest growth rate, followed by the mode with radial order $n_{\mathrm{d}} - 2$, and so on.

Since the fundamental mode properties depend intrinsically on the interior structure, an equivalent modelling is not as simple. However, models show that it usually becomes dominant when the 1O mode has already exceeded the acoustic cut-off, at least for $M \lesssim 3\,\mathrm{M}_{\odot}$, so that it fits the scheme discussed above in most cases of interest.

The main difficulty in applying the above algorithm resides in the computation of ν_{ac}. If the approximation of isothermal atmosphere is valid, it can be computed with equation (8), using the values of M, R, and T at the surface. Note, however, that the mechanical boundary condition in the present pulsation model is not defined at the photosphere, but rather at the outermost point of the models, that can be significantly far from R_{phot} (see e.g. the bottom panels of Fig. 5). As an additional complication, a knowledge of the surface values of μ and Γ_1 is in principle required to employ equation (8). In general, one can assume that $\mu \sim \Gamma_1 \sim 1$, but the approximation is not necessarily good for evolved TP-AGB stars that experience

Table 5. Coefficients of equation (10) for the four lowest order overtone modes, for the O-rich case (in which case $a_{\rm C/O} = 0$).

n	1	2	3	4
a_0	+4.0107	+3.5724	+3.2324	+2.9626
$a_{\rm Z}$	− 0.1466	− 0.0874	− 0.1036	− 0.1013
$a_{\rm X}$	− 0.9965	− 0.8453	− 0.8789	− 0.9045
b_0	+1.5521	+1.9692	+1.7961	+1.8182
$b_{\rm X}$	+0.5154	− 0.0715	+0.1301	+0.1424

Table 6. Coefficients of equation (10) for the first and second overtone modes, for the C-rich case.

n	1	2
a_0	+3.8474	+3.3819
$a_{\rm Z}$	− 0.2079	− 0.1486
$a_{\rm X}$	− 1.0222	− 0.7945
$a_{\rm C/O}$	− 0.1613	− 0.0514
b_0	+1.5895	+1.9311
$b_{\rm X}$	+0.4440	− 0.0471

significant changes in composition and molecule formation in the atmosphere.

In order to provide a more easily applicable prescription, we formulate the problem in terms of the critical luminosity $L_{{\rm ac},\,n}$ at which an overtone mode of given radial order n reaches the acoustic cut-off frequency, for given mass and chemical composition. This luminosity can be interpreted as the transition luminosity between dominant pulsation in the modes n and $n-1$. The critical luminosity can be expressed as:

$$\log\left(\frac{L_{{\rm ac},n}}{{\rm L}_{\odot}}\right) = a_{\rm 0,n} + a_{\rm Z,n}\log(Z) + a_{\rm X,n}X + a_{\rm C/O,n}\log\left[\frac{\rm C/O}{({\rm C/O})_{\odot}}\right] + \left[b_{\rm 0,n} + b_{\rm X,n}X\right]\log\left(\frac{M}{{\rm M}_{\odot}}\right). \tag{10}$$

The coefficients for different radial orders n are shown in Table 5 for the O-rich case and in Table 6 for the C-rich case. For O-rich models, $L_{\rm ac}$ does not depend on C/O ($a_{\rm C/O,n} = 0$). For C-rich models, the effect of C/O is appreciable only at low enough values of $T_{\rm eff}$ to allow for significant molecule formation in the atmosphere. The 3O and 4O modes generally reach the acoustic cut-off at relatively small radii and warm surface temperature, so that $L_{{\rm ac},\,n}$ for $n = 3$ and 4 is essentially insensitive to C/O even in C-rich models. We thus provide coefficients of equation (10) for C-rich composition only for $n = 1$ and 2.

One can use equation (10) to compute the luminosity at which a given overtone mode would reach the acoustic cut-off for a given stellar model. By computing it for $n = 1$–4, and comparing the results with the actual luminosity of the model, one is able to tell that all modes for which $L > L_{{\rm ac},\,n}$ are stable and not observable, the highest overtone mode (of radial order, say, $n = n_{\rm d}$) for which $L < L_{{\rm ac},\,n}$ is the dominant, and the remaining modes are likely excited and have ordered growth rates such that ${\rm GR}_{n_{\rm d}} > {\rm GR}_{n_{\rm d}-1} > {\rm GR}_{n_{\rm d}-2} >$ ..., and so on. If $L > L_{{\rm ac},\,1}$, all overtone modes are stable and the fundamental mode is dominant. We recall that this approach is valid only for $M \lesssim 3\,{\rm M}_{\odot}$, above which value one expects the fundamental mode to be dominant at all luminosities in the interval explored here.

4 PULSATION PERIODS

4.1 Dependence of periods upon stellar parameters

In the present section, we discuss the dependence of pulsation periods upon global stellar parameters, focusing on the fundamental mode and on its dependence upon the stellar radius. The latter aspect is particularly interesting since, to a good degree of approximation, pulsation periods are determined by mass and radius via the period–mean density relation. This is commonly expressed in terms of a period–mass–radius (PMR) relation:

$$\log(P/{\rm days}) = a_0 + a_{\rm M}\log\left(\frac{M}{{\rm M}_{\odot}}\right) + a_{\rm R}\log\left(\frac{R}{{\rm R}_{\odot}}\right). \tag{11}$$

Equation (11) provides a convenient mean to predict periods for stellar models given their mass and radius, or to estimate stellar masses based on observed periods and an independent measurement of the stellar radius.

A significant advantage of this approximation is that it is essentially independent of other global stellar properties. In fact, changes in the chemical composition of the envelope have the main effect of changing the effective temperature by modifying the opacity sources, and thus their effect is already incorporated in the stellar radius. Similarly, differences in core mass result in different luminosities, and again the effect is already included in the stellar radius.

Having computed pulsation models for a wide range of stellar parameters, we are able to verify the degree to which this approximation is valid. We find it to be very well verified for overtone mode periods, with deviations safely within ∼1 per cent. The approximation is also generally valid for the fundamental mode, though with larger deviations, up to ∼20 per cent. To show this, we examine the differences in periods, at fixed mass and radius, resulting from changing one other global parameter at a time. In particular, we study the effects of changing the metallicity, the abundance of helium, and the C/O ratio. Additionally we consider the effects produced by different choices of the mixing length parameter $\alpha_{\rm ML}$ in the calculation of models.

Fig. 11 shows the dependence of the fundamental mode period on radius, luminosity, and effective temperature at constant mass, for series of models of several masses. The Hertzsprung–Russel diagram (HRD) for those models is also shown. The interpretation of the diagram is quite straightforward using equation (11) and recalling that $L \propto R^2T_{\rm eff}^4$. At a given luminosity, the more massive models have higher effective temperature [i.e. warmer Hayashi lines, panel (a)], therefore they have smaller radii and shorter periods [panel (b)]. Conversely, at a given effective temperature, more massive models are brighter, have larger radii and longer periods [panel (c)]. Panel (d) shows how models with different masses follow different period–radius relations, in accordance with equation (11).

4.1.1 *Varying metallicity*

If mass is kept fixed, from equation (11) we expect periods to follow the same relation with radius regardless of other stellar properties, such as chemical composition. This is displayed in Fig. 12, showing the effect of varying the envelope metallicity Z when the other parameters are kept fixed (except for the mass fraction of helium, that varies accordingly with Z since X is fixed). In the HRD, the more metal-poor series of models have higher $T_{\rm eff}$ at a given luminosity, implying a shorter period. As expected, the effect is largely removed when periods are shown against the stellar radius [panel (d)], in

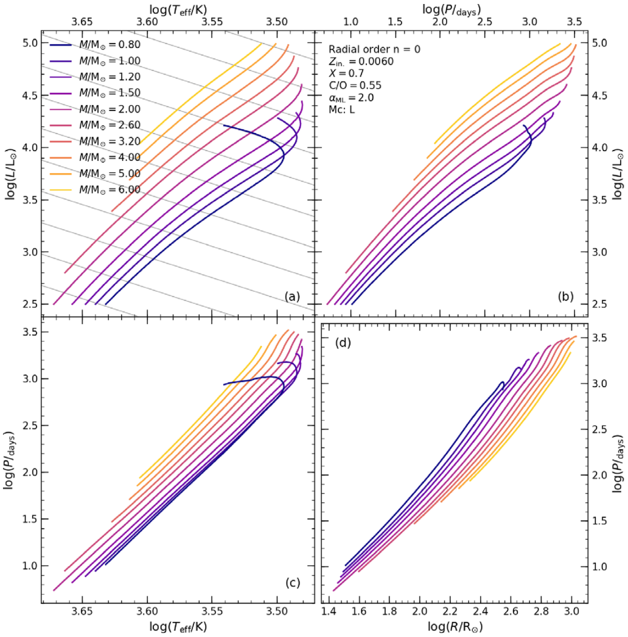

Figure 11. Series of models with $Z = 0.006$, $X = 0.7$, C/O $=$ (C/O)$_\odot$ $\simeq 0.55$, $\alpha_{\rm ML} = 2$, and core mass computed with the 'lower limit' CMLR. Models are shown for masses 0.8, 1.0, 1.2, 1.5, 2.0, 2.6, 3.2, and 4.0 M$_\odot$ (colour coded). Panel (a) shows the models in the HR diagram, while the fundamental mode period P_0 is shown against luminosity [panel (b)], effective temperature [panel (c)], and photospheric radius [panel (d)]. Lines of equal radius are shown in the background of panel (a).

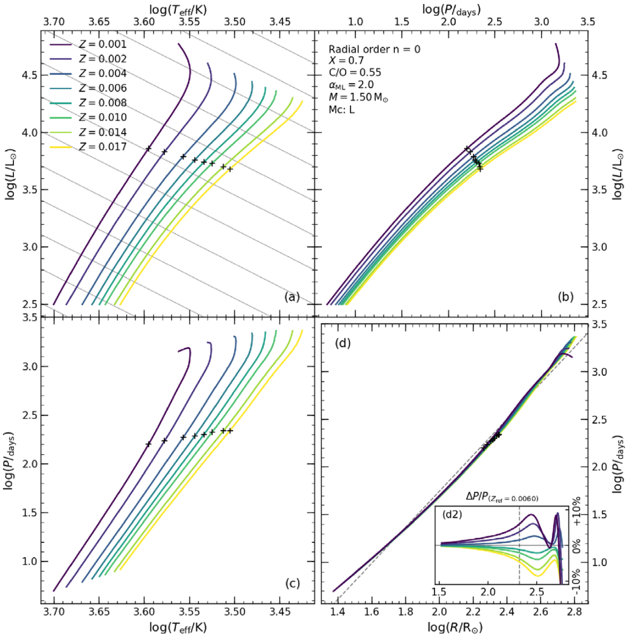

Figure 12. Same as Fig. 11, but only for $M = 1.5\,{\rm M}_\odot$, and displaying series of models with different values of metallicity, (colour coded). The period–radius relations are almost the same, regardless of Z. Inset panel (d2) shows the relative difference in period (with respect to the case $Z = 0.006$ taken as a reference) as a function of log (R/R$_\odot$). Plus symbols mark, along each series of models, the approximate point where the fundamental mode is expected to become excited to a clearly detectable level. The vertical dashed line in panel (d2) has the same meaning.

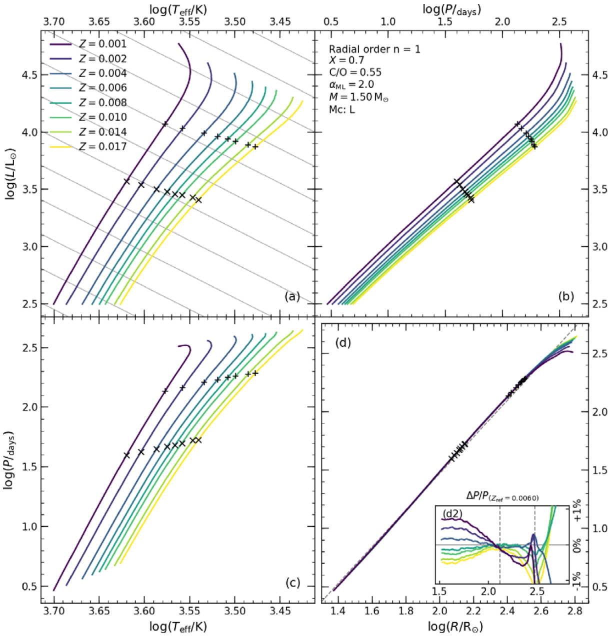

Figure 13. Same as Fig. 12, but for the 1O mode.

which case all series of models lie very close to each other. However, a close inspection reveals that the difference in period between the most metal-rich sequence ($Z = 0.017$) and the most metal-poor one ($Z = 0.001$) can become as large as 20 per cent even though models have the same mass and radius. This is shown in the inset (d2) of panel (d), where the relative period difference (with respect to the series of models with $Z = 0.006$, taken as reference) is displayed as a function of radius. In the case of the 1.5 M$_\odot$ models in Fig. 12, the largest differences occur at $R \sim 250\,{\rm R}_\odot$ and $300 \lesssim P/{\rm days} \lesssim 500$, the range of periods observed in Miras and fundamental mode SRVs. Such differences in period are due to the fact that the coefficients $a_{\rm M}$ and $a_{\rm R}$ in equation (11) are not actually independent of mass and radius. This is discussed in more detail in Section 4.2. In contrast, the relation between period and radius for overtone modes is much more regular, resulting in minute deviations. The largest differences of period at equal radius occur for the 1O mode, for which they are generally smaller than ∼1 per cent (as shown in Fig. 13 for varying metallicity).

4.1.2 Varying helium and hydrogen abundances

Similar considerations, regarding the fundamental mode period, can be made when changing the abundances of hydrogen and helium. Three cases of this situation are considered in the grid of models, obtained with three different values of the hydrogen mass fraction, $X = 0.6$, 0.7, and 0.8. Each case correspond to a different value of He mass fraction as well, determined by $Y = 1 - X - Z$, so that the abundance of helium actually depends upon metallicity in the models. Fig. 14 shows the case for $Z = 0.006$ in which $Y = 0.194$, 0.294, and 0.394. The effect is qualitatively similar to, but less pronounced than, that produced by changing Z, despite of the rather substantial difference $\Delta Y = 0.2$ under consideration.

4.1.3 Varying C/O ratio

The case of varying C/O (Fig. 15) is particularly interesting. During the TP-AGB phase, repeated third dredge-up events bring to the

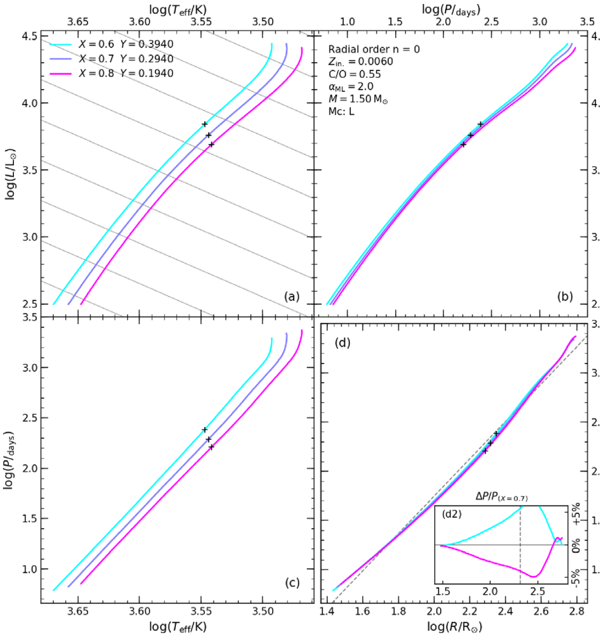

Figure 14. Same as Fig. 12, but with series of models differing in the mass fraction of hydrogen (colour coded).

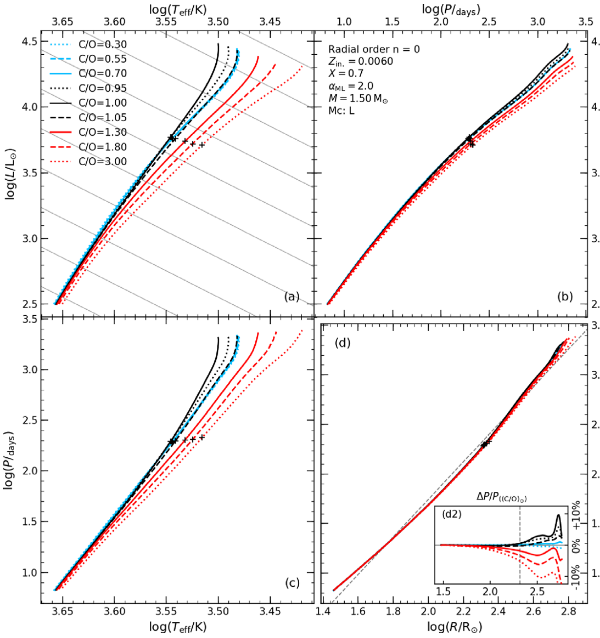

Figure 15. Same as Fig. 12, but with series of models differing in the C/O (colour coded).

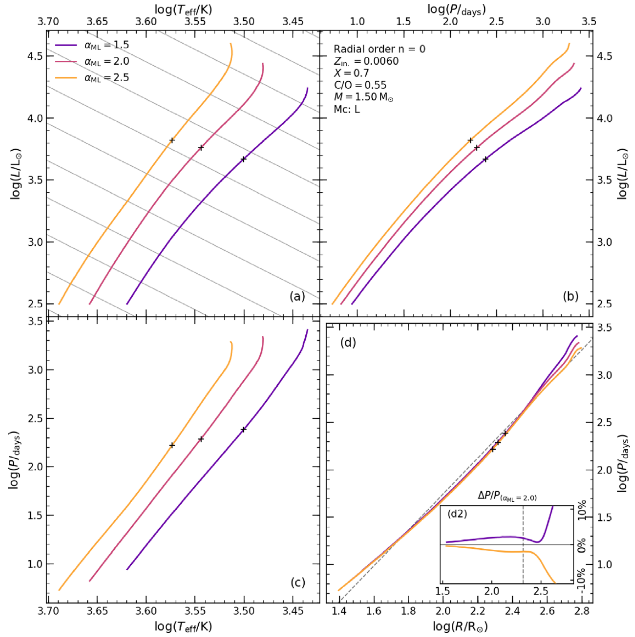

Figure 16. Same as Fig. 12, but with series of models differing in the value of the mixing length parameter $\alpha_{\rm ML}$ used in the computation (colour coded).

surface the products of nuclear burning, enriching the envelope in carbon, and increasing the C/O to values possibly larger than 1, and thus resulting in the formation of carbon stars. When this happens, the sources of molecular opacities in the atmosphere are drastically altered. In fact, owing to the high binding energy of the CO molecule, essentially all carbon atoms in the atmospheres of O-rich stars are locked to form CO, and the low-temperature opacity is dominated by oxygen molecules such as TiO, VO, and H_2O. Conversely, the spectra of carbon stars have strong absorption features of C-bearing molecules (C_2, CN, and SiC), while all the oxygen atoms are locked to form CO (e.g. Marigo & Aringer 2009).

The net result is that, at a given luminosity, C stars have systematically lower effective temperatures than O-rich stars, and thus larger photospheric radii. This can be seen in the HRD [panel (a)] of Fig. 15, where series of models of different C/O are compared. The difference is most evident at high luminosity since the $T_{\rm eff}$ is lower and it is easier to form molecules. It is interesting to observe that the effect of varying C/O is essentially non-existent as long as C/O $\lesssim 0.95$, while the largest temperatures are attained in models with C/O $\simeq 1$ (in which all C atoms as well as the O ones are locked into CO), causing shorter periods. At a given luminosity, models with higher C/O are colder and have longer periods. Conversely, at a given $T_{\rm eff}$, they are less bright and have shorter periods.

At given radius, the relative differences in period are generally small (less than ∼0.5 per cent) when C/O $\lesssim 1$, while the most C-rich models have periods up to 10 per cent smaller than those of O-rich stars.

4.1.4 *Varying α_{ML}*

Finally, we consider the cases of series of models computed with different values of the mixing length parameter (Fig. 16). Models computed with $\alpha_{\rm ML} = 1.5$ are 20 per cent cooler than those in which $\alpha_{\rm ML} = 2.5$ was used, but the effect is largely incorporated in differences in radius, so that at the same radius the fundamental mode periods do not differ by more than ∼5 per cent (having almost doubled $\alpha_{\rm ML}$). Note that the large deviations at $\log{(R/{\rm R}_\odot)} > 2.5$ [Fig. 16, panel (d2)] occur as series of models obtained with a different value of $\alpha_{\rm ML}$ leave the Hayashi line at different radii.

4.2 The period–radius relation of the fundamental mode

In the previous section, we have shown that for overtone modes, theoretical period–radius relations at fixed mass generally fulfill the expectation of being independent of chemical composition and other

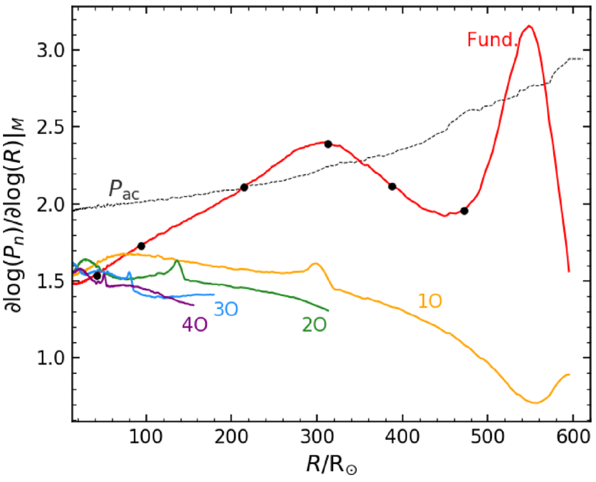

Figure 17. Derivative $\partial\log(P_n/\mathrm{days})/\partial\log(R/\mathrm{R}_\odot)$ as a function of radius for modes in the selected sequence (see Fig. 3 and Table 4). Bumps along lines of overtone modes correspond to the acoustic cut-off, and the dashed line is the derivative of the acoustic cut-off period, $P_{\rm ac} = 1/\nu_{\rm ac}$.

input physics, while the same is not true for the fundamental mode period. Again, this is a consequence of the relatively low sensitivity of the properties of overtone modes to the interior structure of the models. In contrast, the fundamental mode is substantially affected by the conditions in the envelope's interior (see Fox & Wood 1982, in particular their fig. 2). The details of such dependence will be addressed in a forthcoming study. Here, we only point out that a PMR relation in the form equation (11) is not appropriate to describe the period of the fundamental mode.

In fact, the dependence of the fundamental mode period upon stellar radius in the models can be described as a power law only to a first approximation (in other words, $\log(P_0)$ is not exactly linear in $\log(R/\mathrm{R}_\odot)$). Similar considerations can be made for the dependence upon mass. If a functional form such as equation (11) is used to describe fundamental mode periods, the coefficients $a_{\rm M}$ and $a_{\rm R}$ themselves should depend upon mass and radius. In the case of radius dependence, this is evident from Fig. 17, where the local derivative $\overline{a}_{\mathrm{R},n} = \partial\log(P_n)/\partial\log(R)|_M$ of period with respect to radius, at constant mass, is shown for each mode as a function of stellar radius. For overtone modes, $\overline{a}_{\mathrm{R},n} \simeq 1.5$ prior to the cut-off, consistently with the period–mean density relation ($P \propto M^{-1/2}R^{3/2}$). For the fundamental mode, $\overline{a}_{\mathrm{R},0} = 1.5$ at small radii, but then it increases linearly with radius. The trend is not monotonic beyond $R \simeq 300\,\mathrm{R}_\odot$. Note that $\overline{a}_{\mathrm{R},0}$ increases substantially at large radii, doubling its original value.

This dependence of the fundamental period upon radius has two consequences. First, it is the very reason for it never reaching the acoustic cut-off (cf. Fig. 3, top panel; see also the discussion in Section 3.1). Secondly, it produces the deviations described in Section 4.1. The latter fact becomes clear by looking at inset (d2) of Fig. 12 (especially in comparison with Fig. 13): the largest deviations are due to the fact that the same trend of $\overline{a}_{R,0}$ occurs for all metallicities, but at different radii.

4.3 Fitting relations for periods

We provide here best-fitting coefficients for equation (11) to compute pulsation periods of overtone modes as a function of mass and radius (Table 7). Confirming the discussion in the previous sections, the PMR in the form equation (11) allows for a good prediction of overtone mode periods, reproducing values from the models to within ∼10 per cent for the 1O mode, and to within ∼5 per cent or less for higher overtones (see Fig. 18). For each mode, we limited the best-fitting derivation to models in which that mode is dominant according to the prescription provided in Section 3.3, equation (10). Outside such limits, predictions from the best-fitting relations are not necessarily as good.

Table 7. Coefficients of equation (11) for overtone modes periods.

n	1	2	3	4
a_0	− 1.55430	− 1.59749	−1.74684	− 1.84377
$a_{\rm M}$	− 0.52869	− 0.48246	−0.52692	− 0.52069
$a_{\rm R}$	+1.57025	+1.49958	+1.52273	+1.52656

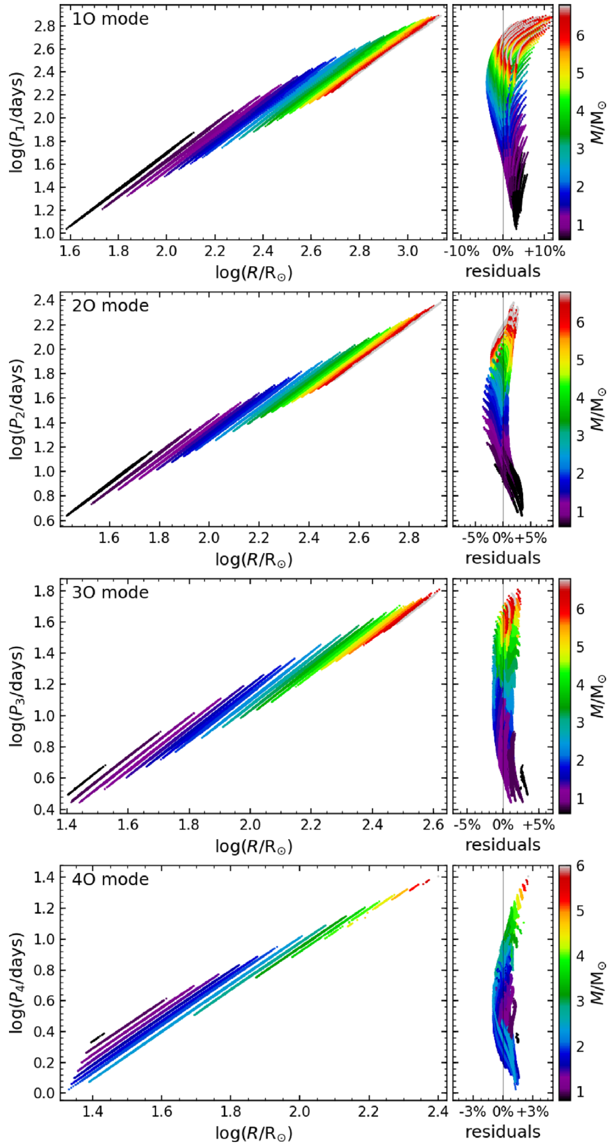

Figure 18. Period–mass–radius relation for overtone modes (left), and residuals of the fitting relations (right). For each overtone n, the plots are limited to models for which $\mathrm{GR}_n > 0$ and the mode is dominant based on equation (10).

Unfortunately, a similarly effective and compact description of the fundamental mode is not possible, for the reasons explained in

Table 8. Coefficients of equation (12) for the fundamental mode period.

a_0	– 1.12166	$c_{\rm M}$	– 0.07659
$a_{\rm M}$	+1.24449	$c_{\rm MR}$	– 0.26130
$a_{\rm R}$	+1.07886	$c_{\rm RM}$	+0.26867
$b_{\rm M}$	+0.87741	$c_{\rm R}$	+0.03278
$b_{\rm MR}$	– 1.53239	$a_{\rm Z}$	– 0.02713
$b_{\rm R}$	+0.10382	$a_{\rm Y}$	+0.14872
		$a_{\rm C/O}$	– 0.01455

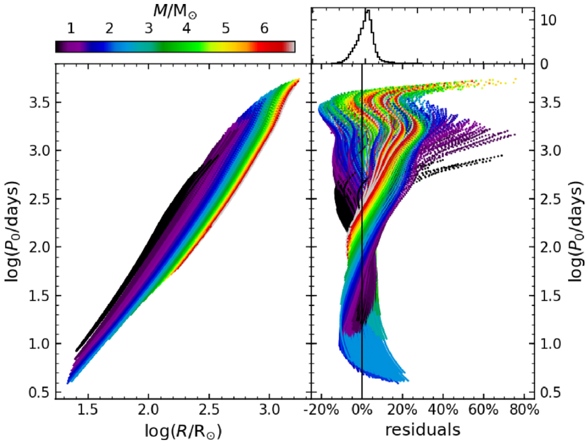

Figure 19. Period–mass–radius relation for the fundamental mode (left), and residuals of the fitting relation (right). Only models which $T_{\rm eff}$ is decreasing with luminosity are shown.

Section 4.2. Also, it is not trivial to limit the derivation of the best-fitting coefficients to a simply defined range of stellar parameters. Here, we provide a reasonable compromise with an expression not too complex but still able to capture the general trend of the models. Since a linear dependence upon $\log{(M/{\rm M}_\odot)}$ and $\log{(R/{\rm R}_\odot)}$ is not valid on the whole range of parameters, we opted for a bicubic form instead. Additionally, we included the dependence upon metallicity, helium mass fraction, and C/O:

$$\begin{aligned}\log(P) = {} & a_0 + a_{\rm M}\tilde{m} + a_{\rm R}\tilde{r} + b_{\rm M}\tilde{m}^2 + b_{\rm MR}\tilde{m}\tilde{r} + b_{\rm R}\tilde{r}^2 \\ & + c_{\rm M}\tilde{m}^3 + c_{\rm MR}\tilde{m}^2\tilde{r} + c_{\rm RM}\tilde{m}\tilde{r}^2 + c_{\rm R}\tilde{r}^3 \\ & + a_{\rm Z}\log(Z) + a_{\rm Y}Y + a_{\rm C/O}\log\left[\frac{\rm C/O}{({\rm C/O})_{\rm ref}}\right], \end{aligned} \qquad (12)$$

where $\tilde{m} = \log(M/{\rm M}_\odot)$ and $\tilde{r} = \log(R/{\rm R}_\odot)$. Best-fitting coefficients are listed in Table 8. Predictions obtained with equation (12) generally match the models periods to within $\lesssim 20$ per cent, except for the high-mass and long-period regime, where significant deviations occur. The residuals from the fit are displayed in Fig. 19. Note that the fit is limited to models for which $\partial\log(T_{\rm eff})/\partial\log(L) < 0$, i.e. models that are cooling down as luminosity increases. The models with the largest positive deviations (around $\log{(P)} \sim 3$) are those for which the structure is already significantly different from a fully convective configuration (they are beginning to depart from the Hayashi line). These models are probably poorly representative of real pulsating stars. The histogram on top of the residuals plot in Fig. 19 shows how the largest majority of models have their periods reproduced to within ∼10 per cent.

5 PULSATION ALONG EVOLUTIONARY TRACKS

In light of the simplified picture of pulsational evolution described above, we examine the behaviour of periods and growth rates for proper evolutionary models. We consider three TP-AGB evolutionary tracks computed with the COLIBRI code (Marigo et al. 2013, 2017), with masses $M_0 = 1.5$, 2.6, and $4.8\,{\rm M}_\odot$, and $Z_0 = 0.008$, where M_0 and Z_0 are the values of total mass and metallicity at the beginning of the AGB phase. Periods and growth rates, computed by interpolation in the grid of pulsation models (see Appendix A1) are displayed in Figs 20–22 as a function of time elapsed since the beginning of TP-AGB.

By looking at the temporal evolution of periods for the $1.5\,{\rm M}_\odot$ and $2.6\,{\rm M}_\odot$ tracks, it is easy to recognize the stability pattern described in Section 3, with the dominant mode gradually shifting towards lower radial orders.[4] On the other hand, the presence of thermal pulses makes hard to identify the familiar pattern of growth rates of Fig. 3, thus justifying the simplified approach employed in the previous sections. In the right-hand panels of Figs 20–22, we show the theoretical PL diagram (PLD), highlighting the location of quiescent evolutionary points.

Using evolutionary tracks, we can examine the role of physical processes ignored in the discussion in the previous sections, such as mass loss and the occurrence of thermal pulses. The effect of mass loss is particularly clear in the PLD of Fig. 20, where we can see that the quiescent evolutionary points bend towards longer periods as luminosity increases, especially for the fundamental mode. In contrast, the evolution of periods with luminosity at constant mass would follow an essentially straight line in the $\log{(P)}$ versus $\log{(L)}$ diagram, similar to that depicted in Fig. 3. In the PLD of Fig. 21, the bending is emphasized by the models transitioning to C-rich, which causes an increase of radius with respect to O-rich models at the same luminosity. A change in slope is particularly evident where C/O $\simeq$ 1. The $4.8\,{\rm M}_\odot$ evolutionary track in Fig. 22 represents a model undergoing HBB. When this process is active, the stellar luminosity is much higher than what predicted by a CMLR in absence of HBB. By providing two values of core mass in the grid of pulsation models, we are able to account for this effect in the estimation of periods and growth rates.

Finally, it is interesting to examine the behaviour of pulsational stability with respect to thermal pulses. In the case of the $1.5\,{\rm M}_\odot$ track, the 1O mode is dominant during most of the quiescent points (marked by vertical lines), with the exception of the last two thermal pulses in which the fundamental mode becomes dominant. In contrast, a substantial portion the $2.6\,{\rm M}_\odot$ track is dominated by 2O mode pulsation. As discussed in Section 3.2, the fundamental mode is virtually always excited and dominant for the $4.8\,{\rm M}_\odot$ evolutionary track. Interestingly, the dominant mode is not the same during individual thermal pulse cycles (TPCs). This behaviour is largely determined by the fact that the star shrinks immediately following a thermal pulse. The decrease in radius causes all pulsation frequencies, as well as the acoustic cut-off frequency (see equation 8), to increase, so that modes that had become stable by exceeding the cut-off are brought back to an unstable configuration. This can be easily understood by imagining that, during the immediate post-flash, models travel backwards along the sequence depicted in Fig. 3.

---

[4] Although not explicitly depicted in the figures, other modes are excited beyond the dominant, in accordance with the fact that LPVs are multiperiodic, at least during part of their existence.

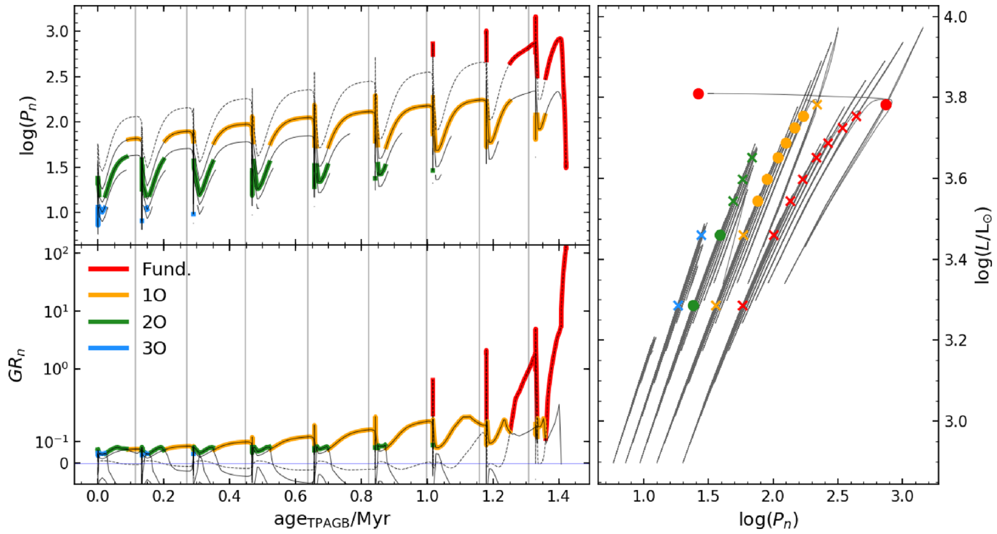

Figure 20. Left-hand panels: periods (top) and growth rates (bottom) as a function of time elapsed since the beginning of TP-AGB in a COLIBRI evolutionary track with $M_0 = 1.5\,\mathrm{M}_\odot$ and $Z_0 = 0.008$ at the beginning of the AGB. Dominant modes are highlighted by thick solid lines in colours. Modes other than the dominant are shown as thin solid lines, except for the fundamental that is shown as dashed thin lines to be more easily distinguishable. Vertical lines mark the point of maximum luminosity of quiescent evolution at each TPC. Note that the 4O mode is never dominant. Right-hand panel: theoretical PLD. Symbols correspond to quiescent evolutionary points, with the dominant mode represented by a filled circle.

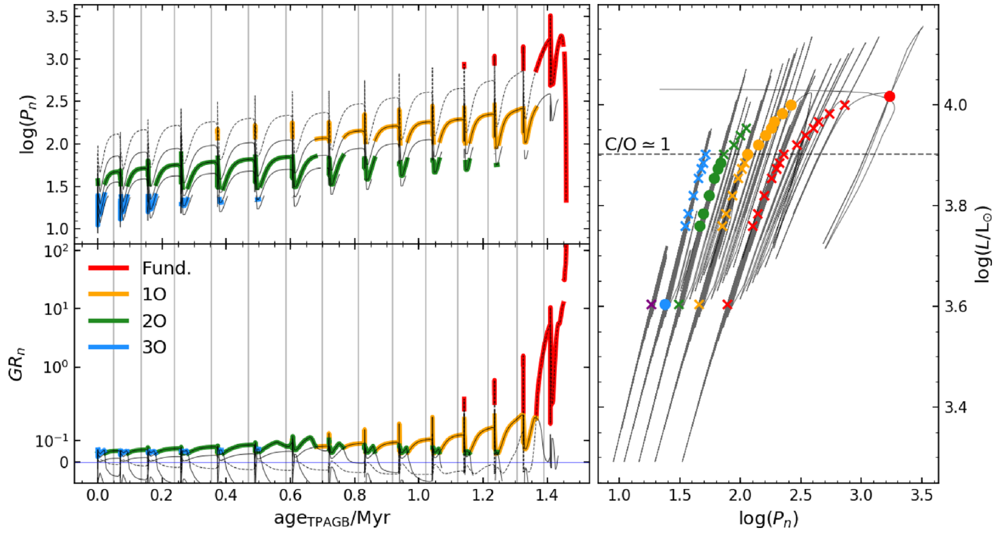

Figure 21. Same as Fig. 20, but for a COLIBRI evolutionary track with $M_0 = 2.6\,\mathrm{M}_\odot$ and $Z_0 = 0.008$ at the beginning of the AGB..

It is instructive to compare the evolutionary tracks discussed above with observations, as shown in Fig. 23. We use variability data for LPVs in the LMC from the OGLE-III data base (Soszyński et al. 2009) combined with *JHK*$_s$ photometry from the Two Micron All Sky Survey (2MASS; Skrutskie et al. 2006). The comparison is made in the K_s–log (P) diagram, where observed PL sequences are most clear. In the left-hand panel of Fig. 23 we show the evolution of the $1.5\,\mathrm{M}_\odot$ track. When its luminosity is low, at the beginning of the TP-AGB, the 3O mode is dominant, with periods on the left edge of sequence A$'$. Upon reaching the acoustic cut-off frequency, the 3O mode becomes stable, and the 2O mode becomes dominant on sequence A. Later, the 1O mode becomes dominant, with periods crossing sequences B and C$'$, and finally the fundamental mode becomes dominant on sequence C. Note, however, that individual modes are not limited to a single sequence (see Trabucchi et al. 2017, and references therein). In fact, the 2O mode is excited (although not dominant) on sequence A$'$ too. Similarly, the 1O mode is excited also on sequence A, and the fundamental mode is found on sequences B and C$'$ as well.

The $2.6\,\mathrm{M}_\odot$ evolutionary track shows a qualitatively similar evolution, with the same correspondence between dominant modes and sequences, but at higher luminosities and longer periods (the variation of mass throughout the PL sequences in the LMC was discussed from an observational point of view in Wood 2015). In this track, as well as the $1.5\,\mathrm{M}_\odot$ one, the fundamental mode is predicted to be dominant with periods longer than those observed on sequence C. This is a direct consequence of the regime of temporary stabilization described in Section 3.1. This disagreement with observations is also discussed in Trabucchi et al. (2017). A detailed analysis of this aspect is beyond the scope of this work, and will be addressed in a forthcoming paper.

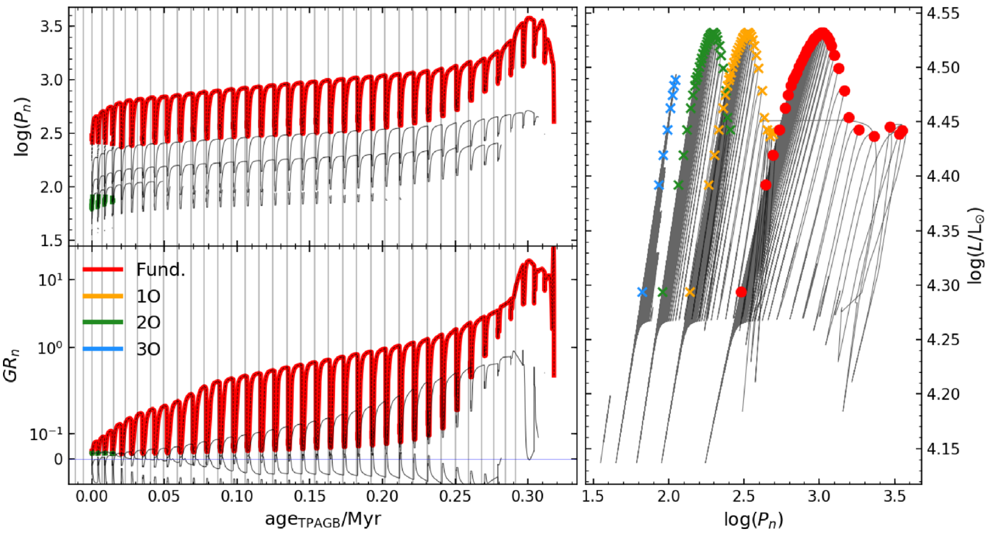

Figure 22. Same as Fig. 20, but for a COLIBRI evolutionary track with $M_0 = 4.8\,{\rm M}_\odot$ and $Z_0 = 0.008$ at the beginning of the AGB.

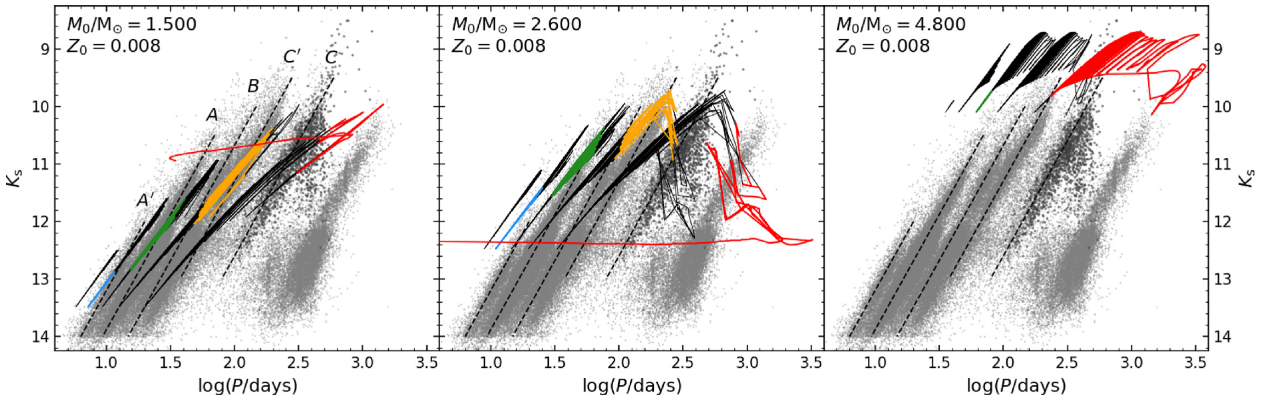

Figure 23. Evolutionary tracks from Figs 20–22 superimposed to the observed $K_{\rm s}$–log (P) diagram of observed LPVs in the LMC, from the OGLE-3 Catalogue (Soszyński et al. 2009). Dashed lines identify the position of observed PL sequences. Observed stars classified as Miras are shown with darker colours on sequence C. For each evolutionary track, the periods of five modes are shown with coloured solid lines where dominant, and black lines otherwise.

The $4.8\,{\rm M}_\odot$ track appears to populate only sequence C, in accordance with the prediction that the fundamental mode is always dominant. Its location is in agreement with that of the brightest Miras in the observed sample. Note that the scarcity of observed stars in that region is compatible with the brief lifetimes of these objects, indeed the $4.8\,{\rm M}_\odot$ evolutionary track has a duration five times shorter than that of the other two (cf. Figs 20–22).

6 CONCLUSIONS

We presented a new grid of linear, non-adiabatic, radial pulsation models for red giant stars, widely covering the space of stellar parameters characteristic of the TP-AGB evolutionary phase. Models include periods and amplitude growth rates for five oscillation modes, from the fourth overtone to the fundamental mode. The grid is made public through a dedicated web interface, the details of which are presented in Appendix A, and represents a significant update with respect to previously published models of LPVs. The main novelty is the exploration of a wide space of chemical compositions in terms of metallicity and C/O ratio, coupled with detailed atomic and molecular opacities consistent with the specific metal mixture assumed for the envelope. This allows for a consistent description of stellar pulsation in stars that experience significant alterations of the envelope composition due to repeated third dredge-up events, and makes the present set of models the first one to systematically account for variability in C-type stars.

We employed models from our grid to provide a general picture of the evolution of pulsation in LPVs, the main results being the following.

(i) The period of overtone modes is determined by global properties mass and radius, and is weakly dependent on other parameters or on the interior structure. Their growth rates are more sensitive than periods to other quantities, but have the interesting properties of dropping to negative values when oscillation frequencies exceed the acoustic cut-off, largely determined by surface properties.

(ii) As a result, overtone modes follow a rather regular pattern, in which the dominant pulsation mode shifts towards lower radial orders as the models expand, and the number of expected excited modes decreases. This tendency is similar to that presented by solar-like oscillation spectra of less evolved red giants.

(iii) In contrast, the properties of the fundamental mode are strongly affected by the internal structure of the models, and in particular by the displacement of the partial ionization zones of major elements associated to the envelope expansion. For this reason, it is much harder to provide a general picture of the fundamental mode as a function of global stellar parameters. For relatively low-mass models ($\lesssim 3\,\mathrm{M}_{\odot}$), the fundamental mode exhibits a regime of temporary stabilization followed by rapid rise in growth rates, and becomes dominant at large radii just after the 1O mode exceeds the acoustic cut-off. In more massive models, on the other hand, it appears to be almost always excited and dominant.

(iv) The period of the fundamental mode is mainly determined by mass and radius, a dependence that can be expressed to a first approximation as $P \propto M^{a_M} R^{a_R}$. However, the power-law exponents a_{M} and a_{R} depend themselves upon mass and radius, in a somewhat erratic fashion. As a consequence, models with different composition and input physics show possibly large deviations from a simple period–mass–radius relation. These properties make it very difficult to derive a best-fitting relation for the fundamental mode period that is both simple and accurate.

(v) We examined in more detail the evolution of pulsation during the TP-AGB by computing periods and growth rates for a few evolutionary tracks, and found the results to be consistent with observations of LPVs in the LMC. The shift of the dominant mode of pulsation towards lower radial orders as stars climb the AGB can be easily put in relation to the observed PL sequences. The radial order of the dominant mode can also change during individual TPCs, as a consequence of the temporary shrinking of the envelope. Pulsation periods, especially for the fundamental mode, are significantly affected by mass loss and by the transition from O-rich to C-rich composition. In both cases, the effect is mainly driven by differences in mass and radius at given luminosity.

(vi) By exploiting the regularity of overtone modes, we provided best-fitting relations for their periods, and a simple prescription to predict the most-likely dominant overtone in a stellar model as a function of global stellar parameters. For not-too-massive models ($M \lesssim 3\mathrm{M}_{\odot}$), the fundamental mode fits this scheme reasonably well. A best-fitting relation for the fundamental mode period is also provided, including the dependence upon chemical composition.

We stress that analytic relations such as those provided here cannot possibly grasp the full complexity of pulsation and its dependence on the properties of stellar models. Therefore, they cannot be used to make accurate predictions, a task for which we encourage the use of the full grid of models and the companion interpolation routine provided via the web interface.

As a next step to expand this work, we plan to include additional values of metallicity to the grid, and to explore the effect of non-scaled-solar oxygen abundances.

In subsequent works, the models computed here will be used to study the pulsation properties, especially the PL sequences, of the populations of red giants in stellar systems. Of particular importance are the LMC, SMC, and the Galactic Bulge where large numbers of red giant variables are known from the OGLE and MACHO surveys, as well as other systems such as globular clusters and local dwarf galaxies.

ACKNOWLEDGEMENTS

We acknowledge the support from the ERC Consolidator Grant funding scheme (*project STARKEY*, grant agreement no. 615604). This publication makes use of data products from the Two Micron All Sky Survey, which is a joint project of the University of Massachusetts and the Infrared Processing and Analysis Center/California Institute of Technology, funded by the National Aeronautics and Space Administration and the National Science Foundation.

REFERENCES

Arnett W. D., 1969, Ap&SS, 5, 180
Baglin A., Auvergne M., Barge P., Deleuil M., Michel E., CoRoT Exoplanet Science Team, 2009, in Pont F., Sasselov D., Holman M. J., eds, IAU Symp. Vol. 253, Transiting Planets. Kluwer, Dordrecht, p. 71
Belkacem K., Goupil M. J., Dupret M. A., Samadi R., Baudin F., Noels A., Mosser B., 2011, A&A, 530, A142
Borucki W. et al., 2009, in Pont F., Sasselov D., Holman M. J., eds, IAU Symposium Vol. 253, Transiting Planets. Kluwer, Dordrecht, p. 289
Borucki W. J. et al., 2010, Science, 327, 977
Brown T. M., Gilliland R. L., Noyes R. W., Ramsey L. W., 1991, ApJ, 368, 599
Caffau E., Ludwig H.-G., Steffen M., Freytag B., Bonifacio P., 2011, Sol. Phys., 268, 255
Chaplin W. J., Miglio A., 2013, ARA&A, 51, 353
Christensen-Dalsgaard J., Kjeldsen H., Mattei J. A., 2001, ApJ, 562, L141
Cox J. P., 1980, Theory of Stellar Pulsation. Princeton Univ. Press, Princeton, NJ
Cox J. P., Giuli R. T., 1968, Principles of Stellar Structure. Gordon and Breach, New York
Dziembowski W. A., Gough D. O., Houdek G., Sienkiewicz R., 2001, MNRAS, 328, 601
Fox M. W., Wood P. R., 1982, ApJ, 259, 198
Freytag B., Liljegren S., Höfner S., 2017, A&A, 600, A137
Höfner S., Olofsson H., 2018, A&AR, 26, 1
Huang C. D. et al., 2018, ApJ, 857, 67
Ireland M. J., Scholz M., Wood P. R., 2008, MNRAS, 391, 1994
Ita Y. et al., 2002, MNRAS, 337, L31
Ita Y. et al., 2004, MNRAS, 347, 720
Keller S. C., Wood P. R., 2006, ApJ, 642, 834
Kiss L. L., Bedding T. R., 2003, MNRAS, 343, L79
Kjeldsen H., Bedding T. R., 1995, A&A, 293, 87
Lattanzio J. C., Wood P. R., 2003, in Habing H. J., Olofsson H., eds, Asymptotic Giant Branch Stars. Springer-Verlag, New York, p. 23
Lebzelter T., Wood P. R., 2007, A&A, 475, 643
Lebzelter T., Wood P. R., 2016, A&A, 585, A111
Marigo P., Aringer B., 2009, A&A, 508, 1539
Marigo P., Bressan A., Nanni A., Girardi L., Pumo M. L., 2013, MNRAS, 434, 488
Marigo P. et al., 2017, ApJ, 835, 77
Menzies J. W., Whitelock P. A., Feast M. W., 2015, MNRAS, 452, 910
Mosser B. et al., 2010, A&A, 517, A22
Mosser B. et al., 2013, A&A, 559, A137
Ostlie D. A., Cox A. N., 1986, ApJ, 311, 864
Percy J. R., Wilson J. B., Henry G. W., 2001, PASP, 113, 983
Rau M. M., Koposov S. E., Trac H., Mandelbaum R., 2018, preprint (arXiv:1806.02841)
Seaton M. J., 2005, MNRAS, 362, L1
Skrutskie M. F. et al., 2006, AJ, 131, 1163
Soszyński I., Udalski A., Kubiak M., Szymański M., Pietrzyński G., Zebruń K., Szewczyk O., Wyrzykowski L., 2004, Acta Astron., 54, 129
Soszyński I. et al., 2009, Acta Astron., 59, 239
Trabucchi M., Wood P. R., Montalbán J., Marigo P., Pastorelli G., Girardi L., 2017, ApJ, 847, 139
Ulrich R. K., 1986, ApJ, 306, L37
Viani L. S., Basu S., Chaplin W. J., Davies G. R., Elsworth Y., 2017, ApJ, 843, 11
Whitelock P. A., Feast M. W., 2014, in Walton N. A., Figueras F., Balaguer-Núñez L., Soubiran C., eds, EAS Publ. Ser. Vol. 67/68, The Milky Way Unravelled by Gaia: GREAT Science from the Gaia Data Releases. EDP Sciences, Les Ulis, p. 263
Whitelock P. A., Menzies J. W., Feast M. W., Nsengiyumva F., Matsunaga N., 2013, MNRAS, 428, 2216

Wood P. R., 1990, in Mennessier M. O., Omont A., eds, From Miras to Planetary Nebulae: Which Path for Stellar Evolution? Editions Frontieres, Gif-sur-Yvette, France,p. 67
Wood P. R., 2000, PASA, 17, 18
Wood P. R., 2015, MNRAS, 448, 3829
Wood P. R., Olivier E. A., 2014, MNRAS, 440, 2576
Wood P. R., Bessell M. S., Fox M. W., 1983, ApJ, 272, 99
Wood P. R. et al., 1999, in Le Bertre T., Lebre A., Waelkens C., eds, IAU Symp. Vol. 191, Asymptotic Giant Branch Stars. Kluwer, Dordrecht, p. 151
Wray J. J., Eyer L., Paczyński B., 2004, MNRAS, 349, 1059
Xiong D.-R., Deng L.-C., 2013, Res. Astron. Astrophys., 13, 1269
Xiong D. R., Deng L., 2007, MNRAS, 378, 1270
Xiong D. R., Deng L., Zhang C., 2018, MNRAS, 480, 2698
Yuan W., Macri L. M., He S., Huang J. Z., Kanbur S. M., Ngeow C.-C., 2017, AJ, 154, 149

APPENDIX A: WEB INTERFACE

The pulsation models can be accessed via the web interface hosted on the web site http://starkey.astro.unipd.it/web/guest/pulsation. The interface allows the computation of pulsation properties for arbitrary combinations of global stellar parameters by linear interpolation in the grid of models (see Appendix A1). The web interface includes the possibility to manually enter the stellar parameters (for individual stellar models) or to upload a properly formatted file containing a tabulated list of the required combinations (for isochrones, evolutionary tracks, or synthetic stellar population models). The whole grid of models, together with the companion interpolation program, is also available for download from the website.

A1 Interpolation routine

The interpolation routine allows the computation of the pulsation properties for a given stellar model represented by a combination of seven global stellar parameters (Z, X, C/O, $M/\mathrm{M}_\odot$, $M_\mathrm{c}/\mathrm{M}_\odot$, $\log(T_\mathrm{eff})$, and $\log(L/\mathrm{L}_\odot)$), that are defined by the user input. Each one of these parameters correspond to one of the dimensions of the grid. The grid is regular in Z_ref, X, C/O, and M, so that the appropriate interpolation nodes can be immediately identified based on the input values. The models are indexed according to their reference metallicity Z_ref, but interpolation is performed over the value of 'true' metallicity (that is stored in the models files). Thus, the input value has to be that of the 'current' metallicity. The corresponding value of Z_ref (used to identify the appropriate interpolation nodes) is computed from Z and C/O as

$$Z_\mathrm{ref} = Z\left\{1 + \left(\frac{X_\mathrm{C}}{Z}\right)_\mathrm{ref}\left[\frac{\mathrm{C/O}}{(\mathrm{C/O})_\mathrm{ref}} - 1\right]\right\}^{-1}, \qquad \mathrm{(A1)}$$

i.e. under the assumption that changes in Z and C/O occur only as a consequence of variations in the abundance of carbon (consistently with the assumptions made in the construction of the grid of models, see Section 2.3). The grid is not exactly regular in core mass, which is related to luminosity by equation (5), so that nodes do not have fixed values. However, this is not an issue since exactly two M_c nodes are available, and thus both used. The most problematic parameter is the T_eff, which value is determined by envelope integration for a given set of input parameters and a given value if α_ML, thus cannot be known *a priori* from other parameters. To account for this, the interpolation proceeds in a series of successive steps, as follows.

First, the value of Z_ref corresponding to the input Z is computed, and the appropriate interpolation nodes are identified, as well as thus for X, M, and C/O. The resulting four pairs of nodes, plus two nodes of M_c and three nodes of α_ML, correspond to $3 \times 2^5 = 96$ combinations, each one identifying a sequence of models with increasing luminosity. For each series of models, the nodes of luminosity bracketing the input value $\log(L_\mathrm{IN})$ are identified, and linear interpolation over those nodes is performed for all periods and growth rates, as well as for M_c and $\log(T_\mathrm{eff})$. The values of M_c computed this way are then used as interpolation nodes in that dimension of the grid. The same operation is then performed for M, C/O, X, and Z in this order, At each step, a new value of $\log(T_\mathrm{eff})$ is also computed. In the end, one is left with three values of $\log(T_\mathrm{eff})$, corresponding to the three α_ML nodes, and the associated values of periods and growth rates, resulting from the successive interpolation. The two nodes of effective temperature bracketing the input value are identified, and a final linear interpolation is performed.

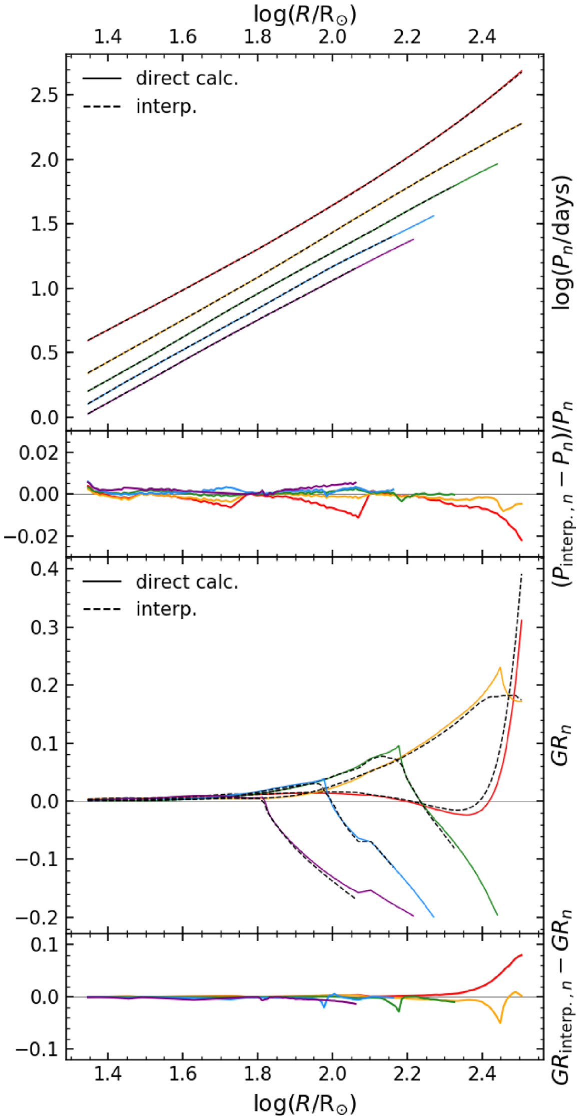

Figure A1. Comparison between periods and growth rates obtained by direct calculation and by linear interpolation over the grid of pulsation models. Periods are essentially indistinguishable between the two approaches. Although differences are visible for growth rates, results from the interpolation reproduce qualitatively well those from direct computation.

Note that the interpolation routine allows for extrapolation wherever the input value is outside the grid boundaries, which are often not known a priori (e.g. for the T_eff, or for $\log(L)$, where the boundaries depends upon mass and chemical composition). Occurrences of extrapolation are recorded in a flag variable that is returned together with the interpolated values of periods and growth rates. The flag distinguishes between extrapolation ‘upwards’ or ‘downwards’. Estimates of pulsation properties for which any extrapolation occurred should be treated with some care. For typical input values, it is not infrequent to obtain extrapolation to lower masses, higher metallicity, or higher or lower values of core mass, luminosity, and $T_{\rm eff}$. A number of tests suggest that extrapolated values are generally safe (provided the input values are not too extreme), with the exception of extrapolation towards luminosity higher than the grid limits, in which case the result is likely unreliable.

A simple way to test the interpolation scheme is to attempt to recover the results of direct computation. An example of this test is shown in Fig. A1. There, we display the periods and growth rates of a series of models specifically computed in which all parameters corresponding to grid nodes vary continuously and monotonically, keeping values within the boundaries of the grid. The corresponding values of periods and growth rates, computed by interpolation over the grid for each model of the series, are also shown there, as well as the differences between the two cases.

Periods are mostly recovered to within less than 1 per cent, a result largely due to the fact that $\log(P_n)$ shows a monotonic dependence upon all parameters, and that dependence is rather close to linear (locally). Growth rates, on the other hand, do not depend monotonically upon global stellar parameters, leading to less accurate results from the interpolation. This is especially true in the neighbourhood of the acoustic cut-off, where growth rates form a cusp that is displaced in luminosity (radius) for different values of mass and chemical composition (as discussed in Section 3.2).

This paper has been typeset from a TEX/LATEX file prepared by the author.